A Coupled-Mode Shallow-Water Model for Tidal Analysis: Internal Tide Reflection and Refraction by the Gulf Stream

SAMUEL M. KELLY

Large Lakes Observatory and Department of Physics, University of Minnesota Duluth, Duluth, Minnesota, and Department of Mechanical Engineering, Massachusetts Institute of Technology, Cambridge, Massachusetts

PIERRE F. J. LERMUSIAUX

Department of Mechanical Engineering, Massachusetts Institute of Technology, Cambridge, Massachusetts

TIMOTHY F. DUDA

Applied Ocean Physics and Engineering, Woods Hole Oceanographic Institution, Woods Hole, Massachusetts

PATRICK J. HALEY JR.

Department of Mechanical Engineering, Massachusetts Institute of Technology, Cambridge, Massachusetts,

(Manuscript received 12 January 2016, in final form 29 June 2016)

ABSTRACT

A hydrostatic, coupled-mode, shallow-water model (CSW) is described and used to diagnose and simulate tidal dynamics in the greater Mid-Atlantic Bight region. The reduced-physics model incorporates realistic stratification and topography, internal tide forcing from a priori estimates of the surface tide, and advection terms that describe first-order interactions of internal tides with slowly varying mean flow and mean buoyancy fields and their respective shear. The model is validated via comparisons with semianalytic models and nonlinear primitive equation models in several idealized and realistic simulations that include internal tide interactions with topography and mean flows. Then, 24 simulations of internal tide generation and propagation in the greater Mid-Atlantic Bight region are used to diagnose significant internal tide interactions with the Gulf Stream. The simulations indicate that locally generated mode-one internal tides refract and/or reflect at the Gulf Stream. The redirected internal tides often reappear at the shelf break, where their onshore energy fluxes are intermittent (i.e., noncoherent with surface tide) because meanders in the Gulf Stream alter their precise location, phase, and amplitude. These results provide an explanation for anomalous onshore energy fluxes that were previously observed at the New Jersey shelf break and linked to the irregular generation of nonlinear internal waves.

1. Introduction

Although much has been learned about oceanic internal tides in the last few decades, some questions remain unanswered regarding their spatial and temporal variability in shelf-edge regions. Observations of such tidal variability abound and have been associated with seasonal variations, three-dimensional structures, remote internal tide generation, and intermittent local mixing as reported, for example, by Holloway (1984), Lerczak et al. (2003), Sharples et al. (2007), Kurapov et al. (2010), and Jackson (2012). Reviews by Huthnance (1995), Hollaway (1988), Ivey (2011), Nash et al. (2012b), Lamb (2014), and others have emphasized that shelf-edge tidal dynamics are challenging to explain because many interconnected processes occur at the shelf break. Particularly strong variability has been documented in the Mid-Atlantic Bight (MAB) region (e.g., Colosi et al. 2001; Nash et al. 2012a). In the present paper, an efficient reduced-physics model that incorporates dominant interaction terms for internal tide dynamics is developed and applied to study internal tide variability specific to this MAB region.

Corresponding author address: Samuel M. Kelly, Large Lakes Observatory, University of Minnesota Duluth, 2205 E 5th Street, Duluth, MN 55812.
E-mail: smkelly@d.umn.edu

DOI: 10.1175/JPO-D-16-0018.1

Our study of internal tide variability builds upon comprehensive field data and model products from the MAB region during the Shallow Water 2006 (SW06) and 2006 Autonomous Wide Aperture Cluster for Surveillance (AWACS) experiments (Tang et al. 2007; Chapman and Lynch 2010). During these experiments, numerous oceanographic and acoustic measurements were collected from July through September 2006 (Newhall et al. 2007; Lynch and Tang 2008; Colosi et al. 2012), and primitive equation forecasts with data assimilation, reanalyses, and adaptive sampling recommendations were issued in real time using the Multidisciplinary Simulation, Estimation, and Assimilation System (MSEAS; Lermusiaux et al. 2006; Haley and Lermusiaux 2010; Lin et al. 2010; Colin et al. 2013). Afterward, more than 1400, implicit, two-way-nested primitive equation reanalyses were completed to improve all aspects of the field estimation. Quick-look evaluations of these simulations led to the detection of sustained interactions between internal tides and the Gulf Stream. Kelly and Lermusiaux (2016) examined some of these interactions using the data-driven primitive equation MSEAS model. One of the conclusions of this analysis was that leading-order tide–Gulf Stream interactions could be explained by first-order mean flow terms acting on mode-1 internal tides. Specifically, subtidal velocities and density gradients associated with the Gulf Stream led to internal tide refraction/reflection and produced regions of anomalous energy-flux divergence and convergence. These results suggested, but did not confirm, that mode-1 tides could originate along the shelf break, reflect at the Gulf Stream, and return to the shelf break to shoal.

Coincidentally, Nash et al. (2012a) observed a superposition of locally generated (offshore propagating) and incident (onshore propagating) internal tides at the New Jersey shelf break during the SW06 experiment. Specifically, Nash et al. (2012a) separated the locally generated and incident internal tides by their coherence and noncoherence, respectively, with the local surface tide. Although Nash et al. (2012a) could not identify the source of the incident internal tides, they emphasized their importance in the generation of large-amplitude nonlinear internal waves that were observed on the New Jersey shelf (Moum and Nash 2008; Shroyer et al. 2009, 2010a,b,c, 2011).

In the present paper, we describe and apply the hydrostatic, coupled-mode, shallow-water model (CSW) to determine whether internal tide reflection at the Gulf Stream is a likely explanation for the incident noncoherent internal tides observed at the New Jersey shelf break. The reduced-physics model is designed for the analysis of first-order tide–mean flow interactions. To this end, CSW describes the horizontal propagation of waveguide (vertical) internal tide modes, under the assumption of first-order mean flow advection but incorporating lateral variability through vertical-mode topographic coupling and the first-order effects of mean flow advection and mean buoyancy variability and their respective shear. The reduced-physics model is efficient because it (i) utilizes a priori estimates of surface tides and subtidal flows, (ii) includes only the dominant tide–mean flow and tide–mean buoyancy interactions, and (iii) uses modes as vertical coordinates. CSW is, however, not intended to replace primitive equation models, which are required where tidal flows are highly nonlinear, wave–wave interactions are important, or strong feedbacks occur between the tide and mean flow. A second aim of this paper is to compare CSW simulations with idealized analytical solutions and primitive equation simulations in varied shelf-edge regions so as to probe the robustness of CSW's dynamical approximations.

Section 2 presents derivations of modal momentum and energy equations that describe internal tide generation, propagation, and scattering in the presence of realistic topography, stratification, and subtidal background ocean. Sections 3 and 4 describe the numerical implementation of CSW and trial simulations, respectively. Section 5 discusses realistic simulations of internal tide generation and propagation in the Gulf Stream region. Section 6 contains a summary and conclusions.

2. Derivation of the coupled-mode shallow-water model

Here, we derive momentum and energy conservation equations for a coupled, normal-mode, shallow-water model. We start with an unforced linear system over arbitrary topography, add a surface tide forcing term, and finish by including first-order tide–mean flow interactions.

a. Unforced and linear dynamics

Internal tides can be described as linear waves provided $u/c \ll 1$ (Pedlosky 2003), where $u \lesssim 0.1\,\mathrm{m\,s^{-1}}$ is a typical tidal current and $c \gtrsim 1\,\mathrm{m\,s^{-1}}$ is a typical phase speed. Finite-amplitude nonlinear effects, which we neglect in this subsection, are important where internal tides produce strong currents (e.g., the South China Sea; Alford et al. 2015) and/or small-scale variability (Zhang and Duda 2013; Duda et al. 2014). Ignoring finite-amplitude nonlinear terms, the inviscid, hydrostatic, Boussinesq equations of motion are

$$\frac{\partial \mathbf{u}}{\partial t} + f\hat{\mathbf{k}} \times \mathbf{u} = -\nabla p, \tag{1a}$$

$$0 = -\frac{\partial p}{\partial z} + b, \tag{1b}$$

$$\frac{\partial b}{\partial t} + wN^2 = 0, \quad \text{and} \tag{1c}$$

$$\nabla \cdot \mathbf{u} + \frac{\partial w}{\partial z} = 0, \tag{1d}$$

where $\mathbf{u}$ is horizontal velocity; w is vertical velocity; p is reduced pressure (i.e., dynamic pressure divided by reference density); $b = -g(\rho - \rho_0)/\rho_0$ is buoyancy perturbation; $\hat{\mathbf{k}}$ is the unit vector in the vertical; ρ and ρ_0 are instantaneous and reference density, respectively; and N and f are the buoyancy and inertial frequencies, respectively. The vertical domain extends from the seafloor at $z = -H(\mathbf{x})$ to the surface at $z = 0$.

The explicit depth dependence at each horizontal location is eliminated by projecting the equations of motion onto vertical modes that are the solutions to the eigenvalue problem:

$$\frac{\partial^2 \Phi_n}{\partial z^2} + \frac{N^2}{c_n^2}\Phi_n = 0. \tag{2}$$

Gill and Clarke (1974) provide a brief history of vertical-mode decompositions, which define the surface tide (barotropic tide) as the zeroth mode and the internal tide (baroclinic tide) as higher modes. In most locations, internal tidal energy and energy flux occur at the longest allowable vertical length scales, so these quantities are efficiently represented by the lowest few modes (e.g., $n < 10$; Nash et al. 2006; Alford and Zhao 2007).

Boundary conditions are required to determine Φ_n. Internal tides approximately obey a rigid lid (i.e., $\Phi_n = 0$ at $z = 0$; Pedlosky 2003); however, decomposing flows that obey a linear free surface using modes that obey a rigid lid results in spurious surface to internal tide energy conversion (e.g., Kelly et al. 2010). Here, we avoid this problem by only considering flows that also obey a rigid lid. The dynamical trade-off is that the equations of motion no longer describe the propagation of surface tides (i.e., their wavelength becomes infinite), but this limitation is circumvented in section 2b by treating surface tides as ''known'' forcing terms. Alternatively, one can define a complete set of modes that explicitly obey a linear free surface. These modes have more complex orthogonality conditions, but they completely eliminate spurious energy conversion and eventually lead to the same expressions for momentum and energy conservation that are derived here [i.e., (7) and (9) below; Kelly 2016].

A locally flat-bottom boundary condition is also used to determine the modes (i.e., $\Phi_n = 0$ at $z = -H$), although the flow itself occurs over arbitrary topography and obeys a kinematic boundary condition (i.e., $w = -\mathbf{u} \cdot \nabla H$ at $z = -H$). The mismatch between these boundary conditions leads to topographic coupling, which is physically interpretable as internal tide generation and/or intermodal scattering.

With rigid-lid and flat-bottom boundary conditions, the modes and their vertical derivatives, $\partial\Phi_n/\partial z = \phi_n$, are orthogonal:

$$\int_{-H}^{0} \Phi_m \Phi_n N^2 \, dz = c_n^2 H \delta_{mn}, \quad \text{and} \tag{3a}$$

$$\int_{-H}^{0} \phi_m \phi_n \, dz = H \delta_{mn}, \tag{3b}$$

and it is useful to note that, by definition of (2), $\partial\phi_n/\partial z = -\Phi_n N^2/c_n^2$. Using this normalization, Φ_n has units of length and ϕ_n is dimensionless. The barotropic mode is then defined as $\Phi_0 = 0$, $\phi_0 = 1$, and $c_0 = \infty$. Using these modes as a complete orthogonal basis, the dynamic variables can be rewritten as

$$[\mathbf{u}(\mathbf{x}, z, t), p(\mathbf{x}, z, t)] = \sum_{n=0}^{\infty} [\mathbf{u}_n(\mathbf{x}, t), p_n(\mathbf{x}, t)]\phi_n(\mathbf{x}, z), \tag{4a}$$

and

$$[w(\mathbf{x}, z, t), b(\mathbf{x}, z, t)] = \sum_{n=0}^{\infty} [w_n(\mathbf{x}, t), b_n(\mathbf{x}, t)N^2(\mathbf{x}, z)]\Phi_n(\mathbf{x}, z), \tag{4b}$$

where Φ_n and ϕ_n depend on $\mathbf{x}$ because N^2 and H depend on $\mathbf{x}$ and appear in (2). Note that w_n and b_n do not have the same units as w and b.

After making the above modal Ansatz substitutions, multiplying (1a) by ϕ_n, (1b) and (1c) by Φ_n/c_n^2, and depth integrating produces

$$\frac{\partial \mathbf{U}_n}{\partial t} + f\hat{\mathbf{k}} \times \mathbf{U}_n = -H\nabla p_n - \sum_{m=0}^{\infty} p_m \int_{-H}^{0} \nabla\phi_m \phi_n \, dz, \tag{5a}$$

$$0 = H\frac{p_n}{c_n^2} + Hb_n, \quad \text{and} \tag{5b}$$

$$H\frac{\partial b_n}{\partial t} + Hw_n = 0, \tag{5c}$$

where $\mathbf{U}_n = H\mathbf{u}_n$ is the equivalent volume transport of each mode, although only the zeroth mode produces a true volume transport. Next, the continuity equation [(1d)] is multiplied by ϕ_n and depth integrated. During this step it is necessary to integrate $\partial w/\partial z$ by parts and utilize both Leibniz's rule and the upper and lower boundary conditions:

$$\int_{-H}^{0} \nabla \cdot \left(\sum_{m=0}^{\infty} \mathbf{u}_m \phi_m \right) \phi_n \, dz + \int_{-H}^{0} \frac{\partial}{\partial z} \left(\sum_{m=0}^{\infty} w_m \Phi_m \right) \phi_n \, dz = 0, \tag{6a}$$

$$\nabla \cdot \mathbf{u}_n H + \sum_{m=0}^{\infty} \mathbf{u}_m \cdot \int_{-H}^{0} \nabla \phi_m \phi_n \, dz + \sum_{m=0}^{\infty} w_m \int_{-H}^{0} \left[\frac{\partial}{\partial z} (\Phi_m \phi_n) - \Phi_m \frac{\partial \phi_n}{\partial z} \right] dz = 0, \tag{6b}$$

$$\nabla \cdot \mathbf{u}_n H + \sum_{m=0}^{\infty} \mathbf{u}_m \cdot \nabla \int_{-H}^{0} \phi_m \phi_n \, dz + \nabla H \cdot \mathbf{u}(-H) \phi_n(-H) - \sum_{m=0}^{\infty} \mathbf{u}_m \cdot \int_{-H}^{0} \phi_m \nabla \phi_n \, dz, \tag{6c}$$

$$+ w(0) \phi_n(0) - w(-H) \phi_n(-H) + \sum_{m=0}^{\infty} w_m \int_{-H}^{0} \Phi_m \Phi_n \frac{N^2}{c_n^2} dz = 0, \quad \text{and}$$

$$\nabla \cdot (H \mathbf{u}_n) - \sum_{m=0}^{\infty} \mathbf{u}_m \cdot \int_{-H}^{0} \phi_m \nabla \phi_n \, dz + H w_n = 0. \tag{6d}$$

Last, (5) and (6d) can be combined to write

$$\frac{\partial \mathbf{U}_n}{\partial t} + f \hat{\mathbf{k}} \times \mathbf{U}_n = -H \nabla p_n - \sum_{m=0}^{\infty} H p_m \mathbf{T}_{mn}, \quad \text{and} \tag{7a}$$

$$\frac{\alpha_n}{g} \frac{\partial p_n}{\partial t} = -\nabla \cdot \mathbf{U}_n + \sum_{m=0}^{\infty} \mathbf{U}_m \cdot \mathbf{T}_{nm}, \tag{7b}$$

where $\alpha_n \equiv gH/c_n^2$ is a nondimensional-scale factor and $\mathbf{T}_{mn}$ and $\mathbf{T}_{nm}$ are topographic coupling coefficients,

$$\mathbf{T}_{mn} = \frac{1}{H} \int_{-H}^{0} \phi_n \nabla \phi_m \, dz, \tag{8}$$

which arise where the vertical structure functions are horizontal variable. The system of (7) is a set of coupled shallow-water equations that describe linear motions over arbitrary topography. An analogous set of equations was previously derived by Griffiths and Grimshaw (2007).

Multiplying (7a) by $\mathbf{u}_n$ and (7b) by p_n and summing produces the mode-n depth-integrated energy equations:

$$\frac{\partial}{\partial t} \left(\frac{H}{2} |\mathbf{u}_n|^2 + \frac{H}{2} \frac{p_n^2}{c_n^2} \right) + \nabla \cdot (\mathbf{U}_n p_n) = \sum_{m=0}^{\infty} C_{mn}, \tag{9}$$

where the terms on the left-hand side are the energy E_n tendency and energy-flux $\mathbf{F}_n = \mathbf{U}_n p_n$ divergence, respectively. Topographic energy conversion from mode m to mode n is

$$C_{mn} = p_n \mathbf{U}_m \cdot \mathbf{T}_{nm} - p_m \mathbf{U}_n \cdot \mathbf{T}_{mn}, \tag{10}$$

as previously derived and applied by Kelly et al. (2012).

b. External forcing

The astronomical tide generating force, which is constant with depth, only significantly forces the surface tide (Hendershott 1981). Therefore, internal tides are generated indirectly where the surface tides scatter at topographic features (Garrett and Kunze 2007). Highly accurate surface tide (mode 0) solutions (e.g., the TPXO7 atlas; Egbert 1997) can be specified a priori to force the baroclinic modes (mode n) by providing estimates of $\mathbf{U}_0$ and p_0 in the topographic coupling terms (i.e., those involving $\mathbf{T}_{mn}$). Because the barotropic mode is constant everywhere ($\phi_0 = 1$), $\nabla \phi_0 = 0$ and $\mathbf{T}_{0n} = 0$. Therefore, the mode-0 (barotropic) tide only forces the mode-n (internal) tide through one term in the summation on the right-hand side of (7b):

$$\mathscr{T}_n = \mathbf{U}_0 \cdot \mathbf{T}_{n0} = -\mathbf{u}_0 \cdot \nabla H \phi_n(-H), \tag{11}$$

where Leibniz's rule has been used. We refer to $\mathscr{T}_n$ as the internal tide generating function (ITGF). The ITGF is similar to the vertical body force derived by Baines (1982) because it depends on surface tide velocity and the topographic gradient. The ITGF depends on the bottom values of the pressure structure functions, which typically do not vary greatly in magnitude. However, the scaling factor α_n in (7b) is proportional to the mode number squared for constant stratification, so the fluid's response to the ITGF decreases rapidly with increasing mode number (analytical calculations of internal tide generation are also known to decrease rapidly with mode number; see Garrett and Kunze 2007).

Topographic mode-n internal tide generation in our linearized system is $C_{0n} = \mathscr{T}_n p_n$. Garrett and Kunze (2007) reviewed internal tide generation in a variety of dynamical settings and concluded that linear dynamics are a good approximation where surface tide excursions are small relative to the dominant topographic length scale (a condition that holds at midocean ridges and

continental slopes). This conclusion is supported by numerous modeling studies that have shown that linear internal tide generation terms dominate nonlinear terms in regional energy balances (e.g., Kurapov et al. 2003; Carter et al. 2008; Kang and Fringer 2012; Buijsman et al. 2014). In contrast, a few high-resolution modeling studies, which resolve extremely short-wavelength internal tides, have shown that nonlinear terms can significantly contribute to generation, even where tidal excursions are small (Gayen and Sarkar 2011; Zhang and Duda 2013). For example, Zhang and Duda (2013) found that nonlinear dynamics reduced generation at a shelf break by 12% in a simulation with 150-m horizontal grid spacing.

c. *Mean flow effects*

Although internal tides with $u/c \ll 1$ propagate as linear waves, they can be steered (Rainville and Pinkel 2006; Park and Watts 2006; Zaron and Egbert 2014; Kelly and Lermusiaux 2016) and scattered (Dunphy and Lamb 2014; Kelly and Lermusiaux 2016) by subtidal flows. Several studies have found that these phenomena appear to be dominated by linearized tide–mean flow interactions, even in fully nonlinear models (Zaron and Egbert 2014; Dunphy and Lamb 2014; Kelly and Lermusiaux 2016).

Following Kelly and Lermusiaux (2016), first-order wave–mean flow and wave–buoyancy interaction terms are included in the modal equations of motion by (i) subtracting the fully nonlinear time-averaged equations of motion from the fully nonlinear equations of motion and (ii) assuming that wave amplitudes are small enough so that wave–wave advection terms can be neglected. This derivation (Kelly and Lermusiaux 2016) does not require a spatial-scale separation between the tides and background flow [e.g., steady flow: $\overline{\mathbf{U}}(x, y, z)$] nor between the tides and horizontally variable background buoyancy [$\overline{B}(x, y, z) = -g(\overline{\rho} - \rho_0)/\rho_0$]. Adding these first-order interaction terms to (7) and neglecting the background vertical velocity lead to

$$\frac{\partial \mathbf{U}_n}{\partial t} + \sum_{m=0}^{\infty} [(\overline{\mathbf{U}}_{mn} \cdot \nabla)\mathbf{U}_m + (\mathbf{U}_m \cdot \nabla)\overline{\mathbf{U}}_{mn} - (\nabla \cdot \mathbf{U}_m)\overline{\mathbf{U}}_{z,mn}] + f\hat{\mathbf{k}} \times \mathbf{U}_n = -H\nabla p_n - H\sum_{m=0}^{\infty} p_m \mathbf{T}_{mn}, \quad \text{and} \tag{12a}$$

$$\frac{\alpha_n}{g}\frac{\partial p_n}{\partial t} + \sum_{m=0}^{\infty}\left(\frac{\alpha_n}{g}\overline{\mathbf{U}}_{p,mn} \cdot \nabla p_m - \frac{\mathbf{U}_m}{c_n^2} \cdot \overline{\mathbf{B}}_{mn}\right) = -\nabla \cdot \mathbf{U}_n + \sum_{m=0}^{\infty} \mathbf{U}_m \cdot \mathbf{T}_{nm}, \tag{12b}$$

where the "effective mean flow" and "effective mean buoyancy" terms (denoted with bars) are computed by projecting the total depth-dependent mean flow [$\overline{\mathbf{U}}(z)$ and buoyancy $\overline{B}(z)$] onto combinations of the structure functions:

$$\overline{\mathbf{U}}_{mn} = \frac{1}{H}\int_{-H}^{0} \overline{\mathbf{U}}\phi_m\phi_n\, dz \quad (\mathrm{m\,s^{-1}}), \tag{13a}$$

$$\overline{\mathbf{U}}_{p,mn} = \frac{1}{H}\int_{-H}^{0} \overline{\mathbf{U}}\frac{N^2}{c_m^2}\Phi_m\Phi_n\, dz \quad (\mathrm{m\,s^{-1}}), \tag{13b}$$

$$\overline{\mathbf{U}}_{z,mn} = \frac{1}{H}\int_{-H}^{0} \frac{\partial \overline{\mathbf{U}}}{\partial z}\Phi_m\phi_n\, dz = \overline{\mathbf{U}}_{p,mn} - \overline{\mathbf{U}}_{mn} \quad (\mathrm{m\,s^{-1}}), \tag{13c}$$

and

$$\overline{\mathbf{B}}_{mn} = \frac{1}{H}\int_{-H}^{0} \nabla\overline{B}\phi_m\Phi_n\, dz \quad (\mathrm{m\,s^{-2}}). \tag{13d}$$

When compared to (7), the three new terms in (12a) represent, from left to right, wave advection by the mean flow, wave interactions with horizontal shear, and wave interactions with vertical shear. Similarly, from left to right, the two new terms in (12b) represent wave advection by the mean flow and wave interactions with horizontal buoyancy gradients.

For simplicity, terms arising through simultaneous topographic and mean flow coupling (i.e., terms describing mean flow effects on topographic scattering) are omitted from the present analysis. Kelly and Lermusiaux's (2016) analyses of fully nonlinear simulations with tides and mean flows indicated that, for the present applications, these terms were less important than the terms retained in (12). In essence, this approximation requires that either topographic or mean flow coupling dominates at any given location.

The energy equations [(9)] with the mean flow terms included then become

$$\frac{\partial E_n}{\partial t} + \nabla \cdot \mathbf{F}_n + \sum_m^{\infty} A_{mn} = \sum_m^{\infty}(C_{mn} + P_{mn}^S + P_{mn}^B). \tag{14}$$

The new terms represent wave–energy advection by the mean flow A_{mn}, shear production P_{mn}^S, and horizontal buoyancy production P_{mn}^B:

$$A_{mn} = [(\overline{\mathbf{U}}_{mn} \cdot \nabla)\mathbf{U}_m] \cdot \frac{\mathbf{U}_n}{H} + \left(\frac{\alpha_n}{g}\overline{\mathbf{U}}_{p,mn} \cdot \nabla p_m\right) p_n, \tag{15a}$$

$$P^S_{mn} = [(\nabla \cdot \mathbf{U}_m)\overline{\mathbf{U}}_{z,mn} - (\mathbf{U}_m \cdot \nabla)\overline{\mathbf{U}}_{mn}] \cdot \frac{\mathbf{U}_n}{H}, \quad \text{and} \tag{15b}$$

$$P^B_{mn} = \left(\frac{\mathbf{U}_m}{c_n^2} \cdot \overline{\mathbf{B}}_{mn}\right) p_n. \tag{15c}$$

d. Tidal analyses

The momentum and energy equations (12) and (14) describe motions and energy exchanges at all frequencies but do not include a mechanism to transfer energy between frequencies (provided the mean flow is steady), that is, narrowband tidal forcing produces narrowband internal tides. Complex tidal amplitudes are extracted via a Fourier transform or by fitting velocity and pressure to tidal harmonics over four tidal periods. Period-averaged covariances, which determine tidally averaged energy and energy flux, are computed $\langle a_n(t)b_n(t)\rangle = \mathrm{Re}(\hat{a}_n\hat{b}_n^*/2)$, where hats indicate complex tidal amplitudes [i.e., $a_n(t) = \mathrm{Re}(\hat{a}_n)\cos(\omega t) + \mathrm{Im}(\hat{a}_n)\sin(\omega t)$] and stars indicate complex conjugates.

3. Numerical implementation

The CSW truncates the system of (7) or (12) at N_m vertical modes and forward integrates the solution on a C grid (i.e., velocity and pressure nodes are staggered in time and space to provide second-order accuracy; Arakawa and Lamb 1977) using a third-order, accurate, Adams–Bashforth, explicit, time-stepping algorithm. Because internal tides propagate relatively slowly, the Courant–Friedrichs–Lewy numerical–stability condition (e.g., Cushman-Roisin and Beckers 2011) permits $O(10–100)$ s time steps.

Forcing is applied by introducing internal tides at the boundaries or through the ITGF [(11)]. Damping is applied via linear/quadratic bottom drags and Laplacian horizontal eddy viscosity. Here, bottom drags are set to zero, and eddy viscosity is chosen using the stability condition $A_H > U\Delta x/2$, where U is a typical tidal velocity and Δx is the horizontal grid spacing (Bryan et al. 1975). Much smaller viscosities are sufficient in simulations with short duration and/or simple topography and mean flows. Sponge conditions at the boundaries damp outward-propagating waves and prevent their reflection (Lavelle and Thacker 2008).

Coriolis terms are difficult to discretize on coarse C grids with "low wave resolution," that is, $\Delta x > 2c_n/f$ (Adcroft et al. 1999). In these regions, numerical errors lead to inaccurate dispersion relations and grid-scale noise. CSW avoids these problems by using a flow-relaxation condition (sponge) at nodes with low wave resolution. This condition preferentially damps high-mode waves in shallow water, which have small eigenspeeds.

Topographic effects in CSW arise through spatially variable eigenspeeds (i.e., c_n or α_n) and topographic coupling terms (i.e., terms involving $\mathbf{T}_{mn}$). The eigenspeeds and vertical structure functions are determined during preprocessing at the pressure nodes by solving the generalized eigenvalue problem [(2)] with realistic $N^2(z)$ and second-order accurate finite differences (e.g., Cushman-Roisin and Beckers 2011). To improve the accuracy of the eigenvalue solution, observed or modeled $N^2(z)$ profiles with irregular vertical grids are linearly interpolated onto a uniform vertical grid prior to solving the eigenvalue problem. Horizontal derivatives in the topographic coupling coefficients [(8)] and ITGF [(11)] are computed using second-order accurate finite differences.

The effective mean flow terms [(13)] are also computed at the pressure nodes during preprocessing. When necessary, topographic and mean flow coupling terms are bilinearly interpolated from the pressure nodes to the velocity nodes at runtime.

4. Trial simulations

a. Topographic coupling

When a constant barotropic transport is applied over subcritical and supercritical continental slopes, CSW produces the qualitative dynamics of internal tide generation (Fig. 1). CSW directly determines the internal tide horizontal velocity and pressure amplitudes, the latter of which is proportional to an "equivalent" surface displacement [$p_n\phi_0(0) = \rho g\eta_n$]. As expected, the pressure amplitudes oscillate in the horizontal, and their wavelengths decrease with mode number and increase with depth. Phase locking between the modal amplitudes leads to vertically propagating internal tide beams in the reconstructed depth profile of pressure over supercritical topography, a well-known qualitative characteristic of the internal tide (Garrett and Kunze 2007).

Although CSW is 3D, we assess its accuracy via comparisons of internal tide generation with the 2D semianalytical Coupling Equation for Linear Tides model (CELT; Kelly et al. 2013) and 2D configurations of the fully nonlinear MIT general circulation model (MITgcm; Marshall et al. 1997). CELT determines internal tide solutions by solving a system of equations (i.e., inverting a matrix) that contains the matching conditions for harmonic vertical-mode amplitudes at

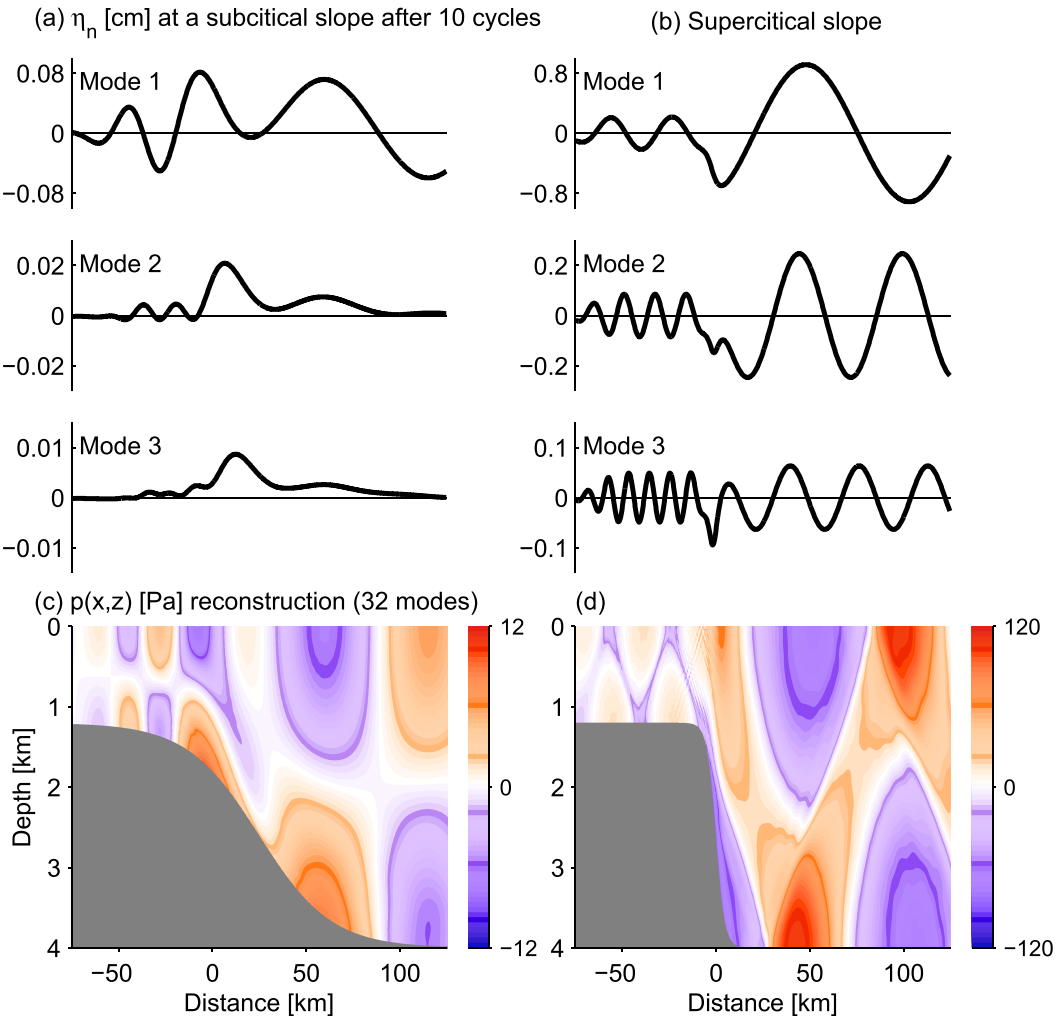

FIG. 1. Snapshots of surface displacements after 10 tidal cycles computed using CSW over (a) subcritical ($s_{max} = 1/2$) and (b) supercritical ($s_{max} = 4$) slopes. Pressure reconstructed from the modal amplitudes [$p(x, z) = \Sigma_n \rho_0 g \eta_n(x)$] displays an internal tide beam when over the (d) supercritical ridge but not the (c) subcritical ridge. The CSW simulations have $\Delta x = 250$ m and $N_m = 32$ modes resolution, $N^2 = 4 \times 10^{-6}\,s^{-1}$ constant stratification, hyperbolic tangent topographic shapes, and are forced with a $U_0 = 100\,m^2\,s^{-1}$ barotropic transport.

discrete topographic steps. Here, the CELT model is inviscid, so internal tide generation is exactly equal to radiated energy flux. Generation in CSW and MITgcm are computed a posteriori by evaluating (10) at each location using model outputs. For the MITgcm simulations, complex modal amplitudes are obtained using least squares harmonic analysis and direct projection of the depth-dependent profiles onto vertical modes (e.g., Kelly et al. 2012, 2013).

Internal tide generation from CSW and CELT agree within ±10% (Fig. 2), except at tall gradual slopes, where CSW indicates that generation is negligible [i.e., $C < 100$ W (m-coastline)$^{-1}$] and CELT is less accurate and requires unfeasibly high vertical and horizontal resolution (i.e., more vertical modes and topographic steps; Kelly et al. 2013).

Internal tide generation from CSW and MITgcm resemble each other in simulations of the Australian (19°S), Oregon (43°N), and New Jersey (39°N) continental slopes (Figs. 3g–i). These locations cover a range of observed stratifications and topographic shapes (i.e., subcritical/supercritical slopes and concave/convex curvature; Fig. 3), suggesting the agreement holds at most locations in the deep ocean, where tidal excursions are small (e.g., Garrett and Kunze 2007). In all three locations, MITgcm and CSW horizontal velocities also qualitatively resemble each other (Figs. 3a–f), despite the former being fully nonlinear and using 500 z levels and the latter being linear and using just 16 modes. Here, the CSW simulations required less than 1% of the

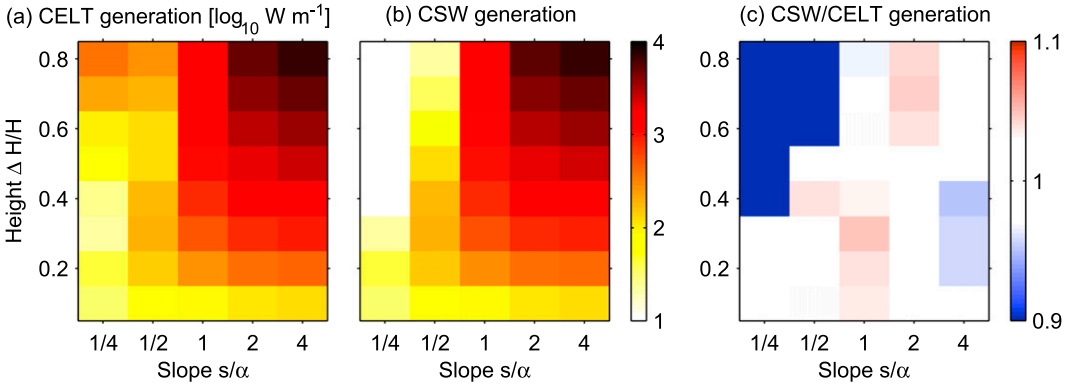

FIG. 2. (a) CELT ($\Delta x = 500$ m, $N_m = 32$ modes) and (b) CSW simulations indicate that slope-integrated, internal tide generation [i.e., W (m-coastline)$^{-1}$] dramatically increases with the height and steepness of the continental slope. (c) The differences between the solutions are ±10%, except at tall gradual slopes where generation is weak.

computation time of the MITgcm simulations (in hydrostatic mode), although the exact speedup is a function of numerous CSW and MITgcm parameters. Of course, CSW is a weakly nonlinear model, which cannot replace a full nonlinear model in regions of strong forcing, where finite-amplitude (i.e., nonlinear wave–wave) advection is important (e.g., Lamb 2004; Legg and Huijts 2006; Venayagamoorthy and Fringer 2006; Zhang and Duda 2013; Lamb 2014).

High- and low-resolution CSW simulations of internal tide generation provide some indications of the model's sensitivity to horizontal and vertical resolution. Generation estimates from low-resolution simulations ($\Delta x = 1$ km and $N_m = 8$ modes) are within ±10% of those

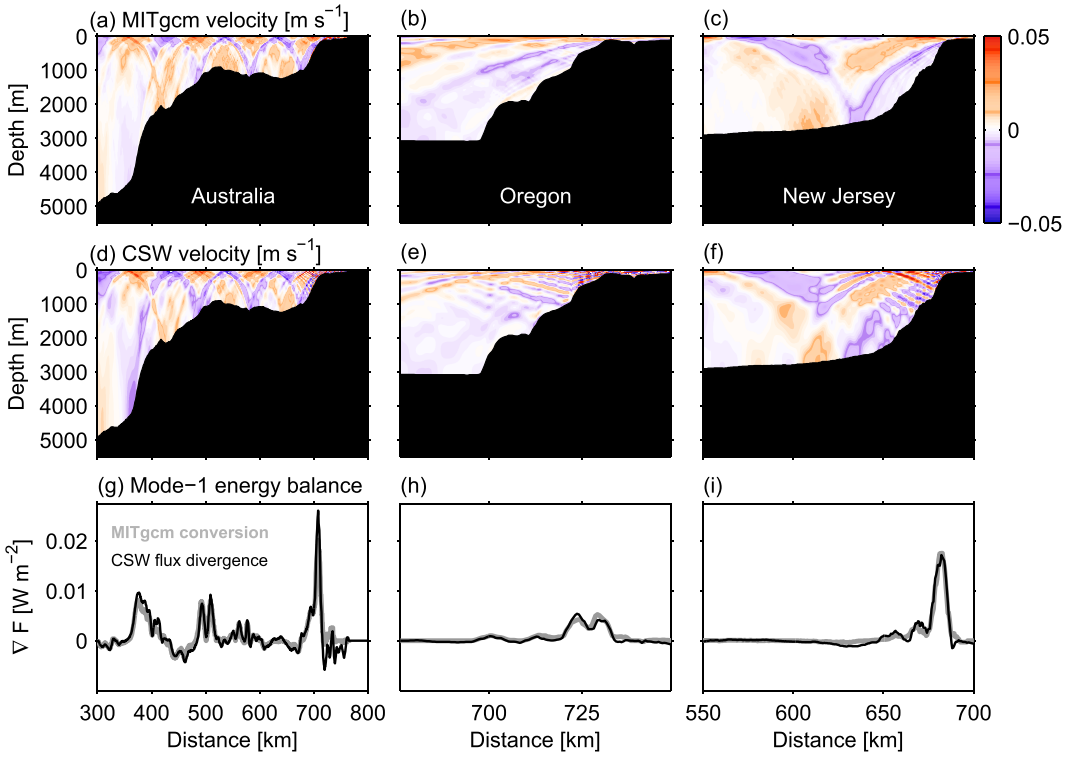

FIG. 3. Internal tide horizontal velocities from six 2D simulations with realistic topography and stratification that are forced with a $U_0 = 100\,\mathrm{m^2\,s^{-1}}$ barotropic transport. (a)–(c) Fully nonlinear simulations using the MIT general circulation model ($\Delta x = 500$ m and $\Delta z = 10$ m) qualitatively resemble the (d)–(f) linear simulations using CSW ($\Delta x = 500$ m and $N_m = 16$ modes). (g)–(i) Internal tide generation in the MITgcm closely matches energy-flux divergence in CSW. The depth structure of the CSW velocities is reconstructed by summing 16 vertical modes.

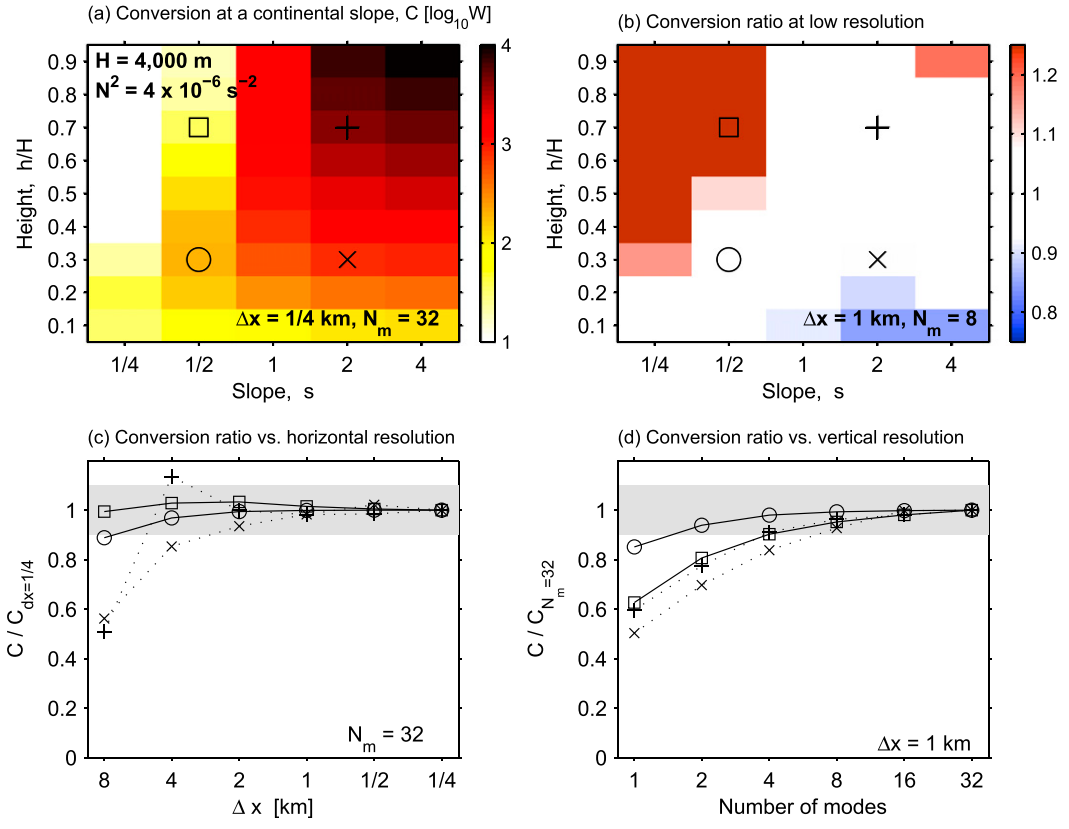

FIG. 4. (a) In high-resolution CSW simulations ($\Delta x = 250$ m and $N_m = 32$ modes), internal tide generation dramatically increases with the height and steepness of the continental slope. (b) In low-resolution simulations ($\Delta x = 1$ km and $N_m = 8$ modes), the ratio of conversion relative to the high-resolution simulations is 0.9–1.1, except at very tall gradual slopes, where total conversion is negligible (i.e., $C < 100$ W). For a variety of slope heights and steepnesses [identified by square, circle, plus, and x symbols in (a) and (b)], internal tide generation converges at around [(a) and (c)] 2-km horizontal resolution and [(b) and (d)] $N_m = 8$ vertical modes. The suite of simulations here has topographic shapes, stratification, and barotropic forcing identical to those shown in Fig. 1.

obtained from the high-resolution simulations ($\Delta x = 250$ m and $N_m = 32$ modes), except at extremely tall gradual slopes, where internal tide generation is small (Figs. 4a,b). For several hyperbolic tangent topographic profiles of moderate heights and steepnesses, internal tide generation converges rapidly once $\Delta x < 2$ km and $N_m > 8$ (Figs. 4c,d). For moderate topographic profiles, the rates of conversion do not depend strongly on the values of height and steepness. The sensitivity analysis here is not exhaustive, but it provides zeroth-order guidance for resolving internal tide dynamics in realistic settings.

b. Mean flow coupling

The advective and vertical shear terms in CSW can be tested by comparing CSW simulations with analytical solutions to the hydrostatic Taylor–Goldstein (TG) equation, which describes nonrotating internal waves of the form $w_{\rm tot} \propto w(z)\exp[ik(x-ct)]$ in a parallel shear flow $\overline{U}(z)$:

$$(c-\overline{U})\frac{\partial^2 w}{\partial z^2}+\frac{\partial^2 \overline{U}}{\partial z^2}w=-ikb, \quad \text{and} \tag{16a}$$

$$(c-\overline{U})ikb=N^2 w. \tag{16b}$$

The TG system of equations is usually presented as a single equation for $w(z)$; however, retaining $b(z)$ and splitting as above allows the system to be rewritten as a generalized eigenvalue problem:

$$c\begin{bmatrix}\dfrac{\partial^2}{\partial z^2} & \mathbf{0}\\ \mathbf{0} & \mathbf{I}\end{bmatrix}\begin{bmatrix}w\\ ikb\end{bmatrix}=\begin{bmatrix}\overline{U}\dfrac{\partial^2}{\partial z^2}-\dfrac{\partial^2\overline{U}}{\partial z^2} & -\mathbf{I}\\ N^2 & \overline{U}\end{bmatrix}\begin{bmatrix}w\\ ikb\end{bmatrix}, \tag{17}$$

where c are the eigenvalues, the concatenation of $w(z)$ and $ikb(z)$ are the eigenfunctions, and $\mathbf{0}$ and $\mathbf{I}$ are the zero and identity matrices, respectively. The problem

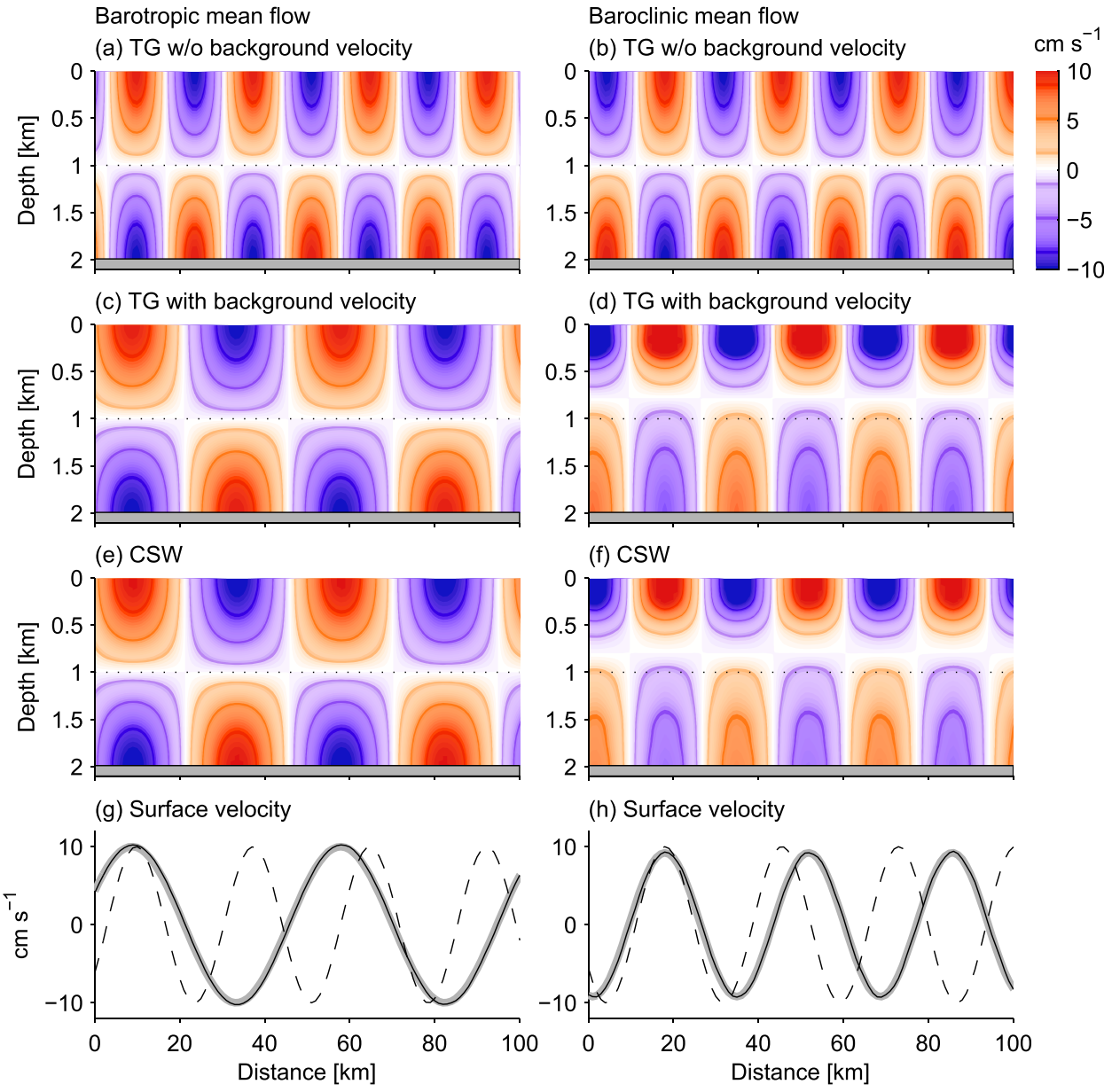

FIG. 5. Internal tide horizontal velocity is shown for (left) barotropic and (right) baroclinic background flows. The flows are determined from the analytical mode-1 TG solutions (c),(d) with and (a),(b) without mean flows and (e),(f) from the CSW simulations with flows initiated using the TG solution at the left boundary. (g),(h) Plots of surface velocity display the close agreement between the TG (black) and CSW solutions (gray) in the presence of a mean flow, and their departure from the TG solutions that neglect the mean flow (dashed).

is discretized and solved analogously to (2). The problem is simpler than the full (nonhydrostatic) TG equation because the eigenvalues are speeds rather than frequencies, and the input matrices do not require a specified wavenumber. In practice, once $w(z)$ and c are found, ω is set to the tidal frequency to determine k, and horizontal velocity is obtained from vertical velocity using the continuity equation $[iku(z) = -\partial w/\partial z]$.

The solutions to the TG equation reveal how mean flows alter the shape and wavelength of the mode-1 internal tide. Here, we consider a fluid with constant stratification and a barotropic mean flow, $\overline{U} = 0.5\,\mathrm{m\,s^{-1}}$, or a baroclinic mean flow, $\overline{U}(z) = 0.25[\tanh(1 + z/200) + 1]\,\mathrm{m\,s^{-1}}$ (i.e., the flow is strong at the surface and nearly zero at the bottom).

Mode-1 waves propagating in the direction of the mean flows increase in horizontal wavelength (Figs. 5a–d).

The surface-intensified baroclinic mean flow also raises the depth of the mode-1 horizontal velocity zero crossing (Fig. 5d). CSW simulations (here with no rotation) are compared with the analytical results by projecting the first TG mode onto flat-bottom modes (the modes defined by 2) and initiating this spectrum at the left boundary of the CSW domain. When terms describing the effects of advection and vertical shear are neglected in CSW, this forcing produces a vertically propagating beamlike structure due to the seemingly random superposition of modes (not shown, but see Fig. 1). However, when mean flow terms are included in CSW, the forcing produces a coherent structure that only propagates horizontally and has the same wavelength and zero crossing as the TG mode (Figs. 5e,f). Horizontal surface velocities reveal the close agreement between the model and theory (Figs. 5g,h).

Last, an idealized two-dimensional MITgcm simulation of a mode-1 internal tide crossing the Gulf Stream tests all of the CSW mean flow terms (Fig. 6). The initial state of the simulations is realistic across-axes slices of Gulf Stream density and horizontal velocity. The simulations are forced with a mode-1 internal tide at the left (onshore) boundary, which propagates across a 2000-km numerical domain. The simulations have 2-km and 20-m horizontal and vertical resolution, respectively. Additional details and analyses of the MITgcm simulation are discussed in Kelly and Lermusiaux (2016). An identically configured CSW simulation replicates the MITgcm patterns of both horizontal internal tide velocity and shear/buoyancy production where the tide crosses the Gulf Stream. The close quantitative agreement of the MITgcm and CSW simulations suggests that mean flow shear and horizontal buoyancy gradient terms are accurately implemented in CSW and that, in this situation, CSW includes the leading-order dynamics at work in a fully nonlinear model.

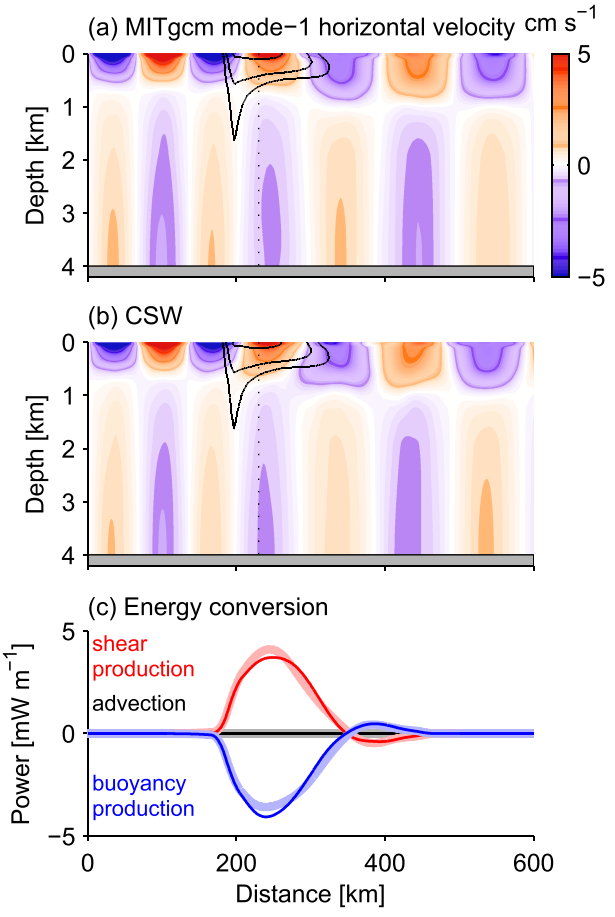

FIG. 6. In (a) MITgcm and (b) CSW simulations, mode-1 internal tide velocity displays a longer wavelength and deeper zero crossing after crossing the Gulf Stream. (c) While crossing the Gulf Stream, shear and buoyancy production approximately cancel each other in both the MITgcm (thick lines) and CSW (thin lines). Gulf Stream velocity contours are shown every 0.25 m s^{-1} (the mean flow is into the page).

5. Application to the Gulf Stream region

a. Idealized internal tide reflection at the Gulf Stream

Kelly and Lermusiaux (2016) utilized data-driven regional nonlinear primitive equation MSEAS simulations to examine interactions between mode-1 internal tides and the shelfbreak front and the Gulf Stream. For the latter, the dominant dynamical term was internal tide advection by the Gulf Stream, suggesting that geometric wave theory could be used to predict internal tide reflection. Here, we validate this finding by using CSW to simulate mode-1 internal tides as they strike a realistic cross section of the Gulf Stream at different angles of incidence (Fig. 7). As predicted by geometric wave theory, incident mode-1 tides at grazing angle $\theta = 30°$ ($\theta = 150°$) undergo specular reflection at the shoreward (seaward) edge of the Gulf Stream by regions of large velocity (eigenspeed). Incident mode-1 tides near the critical angles ($\theta = 60°$ and $\theta = 120°$) reveal the limitations of geometric wave theory by displaying partial reflection and transmission. However, the angles of the reflected and transmitted waves are still accurately predicted by geometric theory. The CSW simulations support the conclusion that mode-1 internal tides' incident at angles $\theta < 60°$ and $\theta > 120°$ are reflected shoreward by the Gulf Stream. However, they do not indicate a binary transition between transmission and reflection at the critical angles.

b. Internal tide reflection, refraction, and scattering by the Gulf Stream

We now analyze the effects of internal tide reflection by the Gulf Stream on the directionality and intermittency of internal tides in the Mid-Atlantic Bight

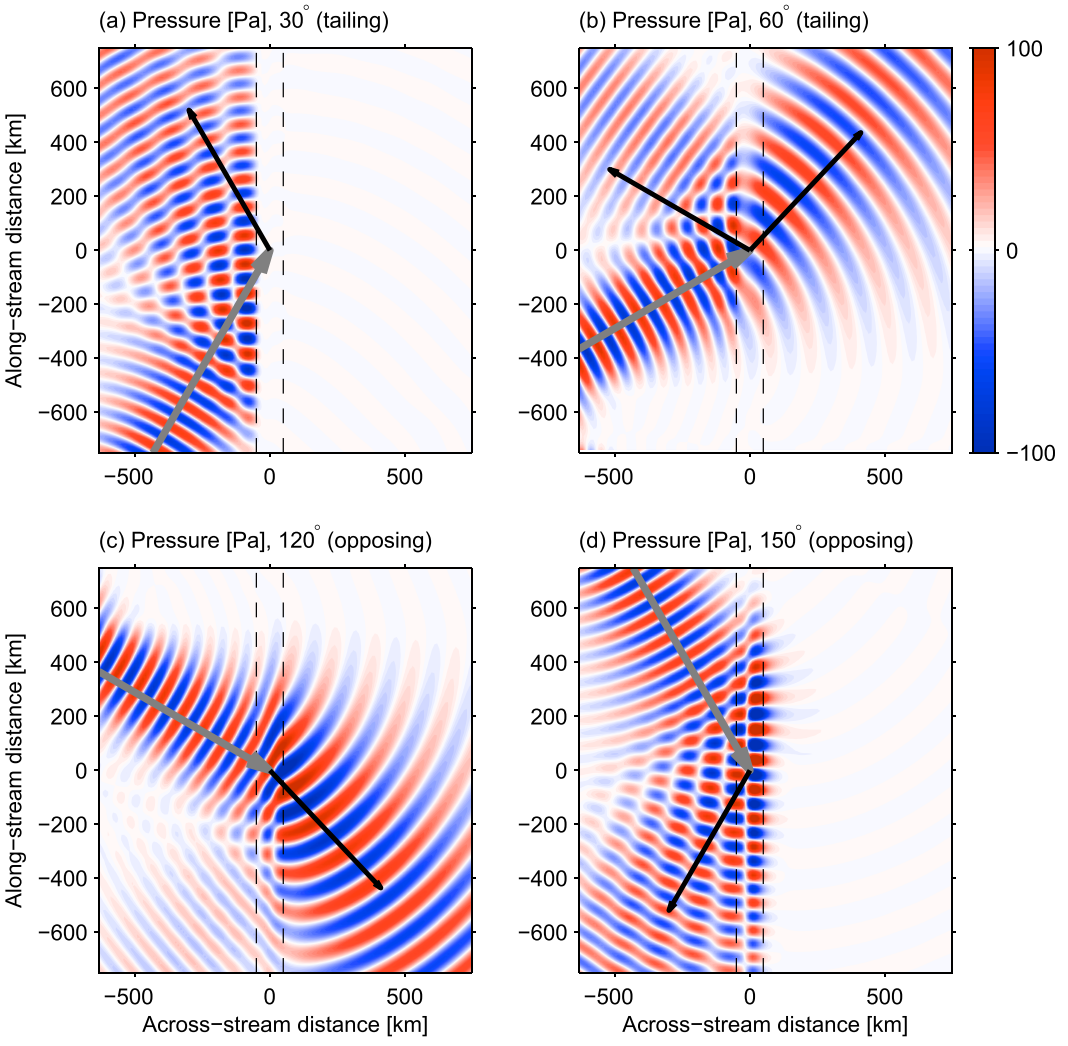

FIG. 7. CSW simulations of mode-1 internal tides incident on the Gulf Stream are visualized through snapshots of mode-1 pressure. The orientation of the incident internal tides is indicated by gray arrows. The orientation of the reflected tides predicted from geometric theory is indicated by black arrows. The Gulf Stream propagates from bottom to top (at an angle of $\theta = 0$) and its horizontal extent is marked by dashed lines. Cross-stream profiles of Gulf Stream phase speed and velocity are presented in Kelly and Lermusiaux (2016).

region. To do so, we study 24 realistic CSW simulations of regional internal tide interactions with the Gulf Stream. The computational domains extend from 30° to 45°N and 60° to 80°W, have 3-km horizontal resolution, and include eight vertical modes. The simulations employ realistic topography (Smith and Sandwell 1997), TPXO M_2 surface tide velocities (for computing the ITGF), and subtidal flows interpolated from a 1/12° global simulation conducted with the Hybrid Ocean Coordinate Model (HYCOM, experiment 19.1; Chassignet et al. 2007). Snapshots of HYCOM data from 20 August 2001–12 provide 12 different summer Gulf Stream conditions. The effect of the Gulf Stream was isolated by running two simulations for each year. The first simulation employed HYCOM background conditions that were low-pass filtered with a 500-km 2D Hanning window to completely eliminate the Gulf Stream (and all other mesoscale variability). The second simulation reintroduced the Gulf Stream by including the high-passed background conditions in offshore regions using a linear weight between the 0- and 3000-m isobaths (i.e., realistic unfiltered HYCOM data were used in regions deeper than 3000 m). In both simulations, filtering the background conditions removed small-scale variability at generation regions (such as the shelfbreak front), which could have provided additional sources of internal tide variability and complicated the analyses of tide–Gulf Stream interactions. A typical map

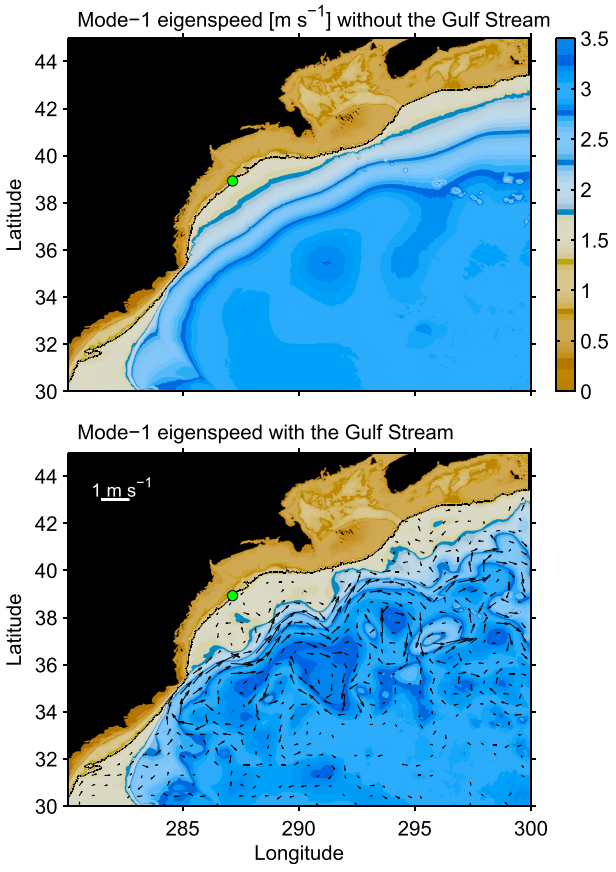

FIG. 8. (a) August 2006 mode-1 eigenspeeds computed from 500-km low-passed HYCOM densities depend on bottom depth and regional stratification. (b) Eigenspeeds computed from unfiltered offshore densities additionally depend on the location of the Gulf Stream and its mesoscale meanders, warm-core rings, and eddies. Vectors represent the effective HYCOM mean flow given by $\overline{\mathbf{U}}_{11}$. A green dot marks the location of the SW06 field experiment on the New Jersey shelf break. The coastline reflects the model bathymetry, which omitted all locations shallower than 30 m.

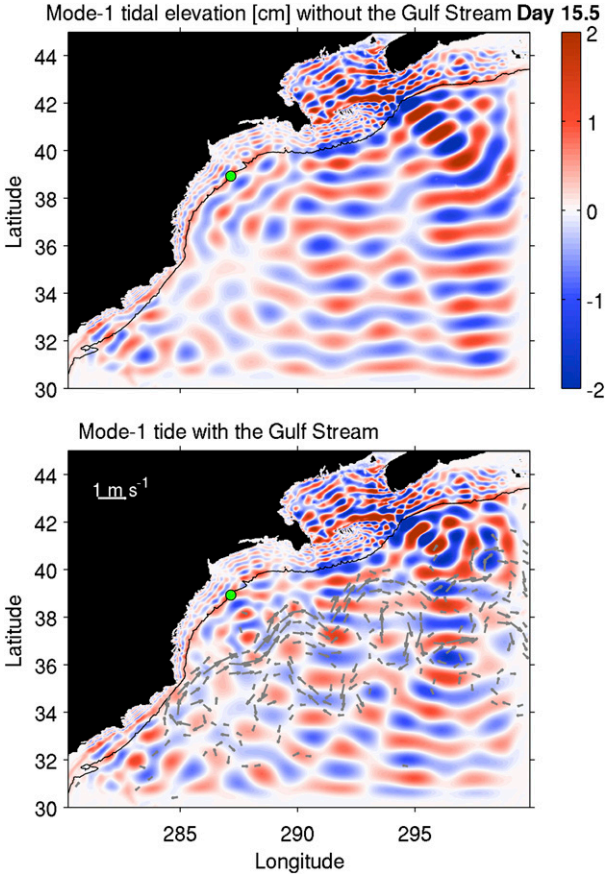

FIG. 9. August 2006 snapshots of CSW mode-1 surface displacements reveal internal tides radiating from the shelf break and offshore interference patterns that are greatly influenced by the Gulf Stream.

of eigenspeed and the effective mean flow indicates that low-pass filtering the HYCOM data effectively removes the Gulf Stream (e.g., eigenspeed in the low-pass filtered simulation is predominantly just a function of depth; Fig. 8).

CSW was integrated for 30 tidal cycles with a steady mean flow. After approximately 20 tidal cycles, the simulations developed instabilities in regions of strong mean flow gradients. This is possible because linearized systems can exhibit unlimited growth even when the underlying nonlinear system is stable, since the neglected higher-order terms can contain the negative feedbacks. The instabilities persisted even after testing a variety of numerical algorithms, perhaps indicating that they are due to physical processes, such as wave capture (Bühler and McIntyre 2005). Consistent with wave capture, the instabilities developed more slowly in test simulations where the mean flow was periodically updated (i.e., varied in time) and were eliminated by omitting the terms in (12) that are responsible for shear and buoyancy production. In the end, the simulations were conducted with horizontally variable eigenspeeds and just the mean flow terms responsible for wave advection (i.e., the terms consistent with the geometric approximation). These simulations retained the dynamics that explain idealized internal tide refraction/reflection at the Gulf Stream (Fig. 7) and the dominant tide–mean flow interactions quantified by Kelly and Lermusiaux (2016).

Snapshots of mode-1 elevation in simulations with and without the Gulf Stream contain similar patterns along the shelf break, particularly on the eastern flank of George's Bank, where energetic internal tides radiate offshore [Fig. 9; also, Chen et al. (2011) simulated a 1.1-GW internal tide radiating away from a ~100-km segment of shelf break northeast of the bank]. The Gulf

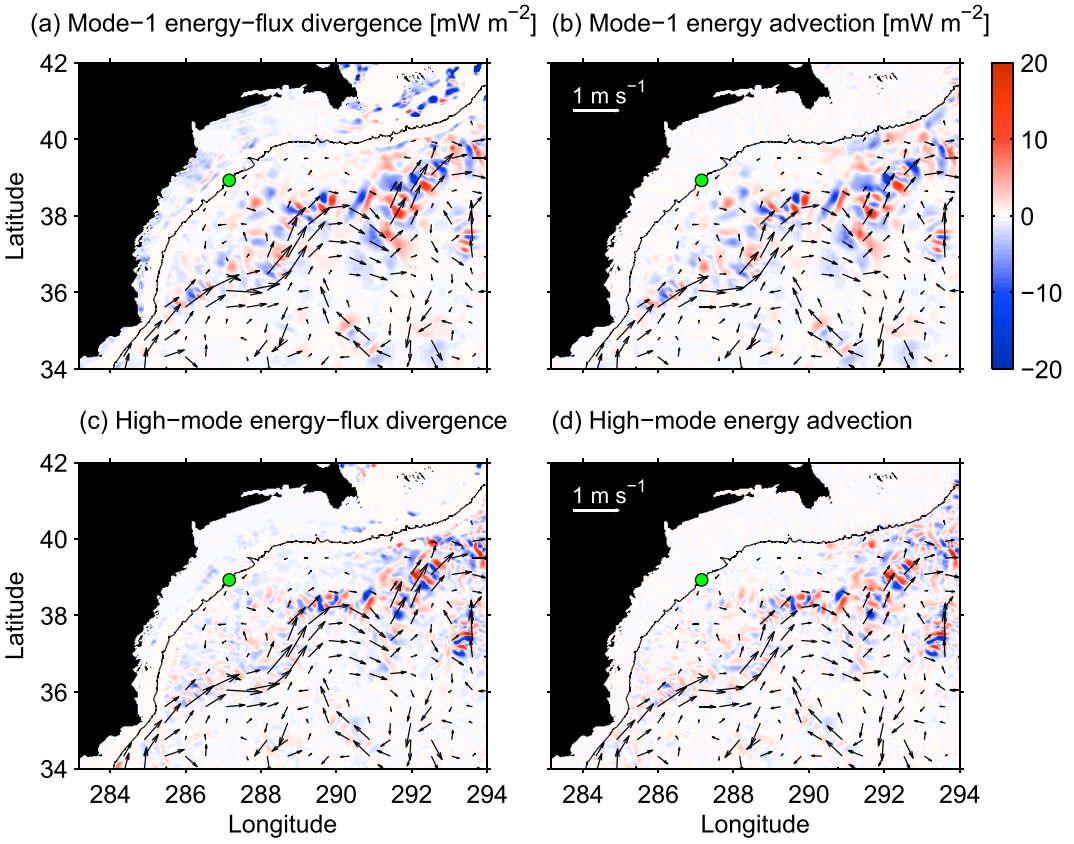

FIG. 10. August 2006 tidally averaged (a) mode-1 and (c) high-mode (n = 2–8) energy-flux divergences in CSW are balanced by tidal energy mean flow advection (15a) in the (b),(d) Gulf Stream away from the steep topography [here the sign of A_{mn} is reversed, so that advection appears as a source term in (14)]. To emphasize mean flow effects, energy-flux divergences are not plotted where topographic generation exceeds 1 mW m^{-2} (i.e., along the shelf break). Vectors represent Gulf Stream velocities [$\overline{\mathbf{U}}_{11}$ in (a) and (b) and $\overline{\mathbf{U}}_{22}$ in (c) and (d)].

Stream drastically alters the propagation of these waves and their interference patterns. Near 40°N, 298°E, the offshore propagating internal tide beam even partly reflects northward where it strikes the Gulf Stream, instead of continuing to propagate southeast toward 38°N, 300°E, as it does in the absence of the Gulf Stream. This situation is reminiscent of the idealized reflection shown in Fig. 7a.

The Gulf Stream's impact on the internal tide energy balance in CSW is quantifiable via A_{mn}, the energy–advection term in (14), which balances tidally averaged, internal tide, energy-flux divergence in the Gulf Stream (Fig. 10; note that P^S_{mn} and P^B_{mn} are not present in these simulations). The pattern produced by $\Sigma_m A_{m1}$ has an amplitude of $O(20)$ mW m^{-2} and a horizontal scale comparable to the wavelength of the mode-1 internal tide. Similarly, the pattern produced by $\Sigma_m A_{mn}$ for all n = 2–8 has horizontal scales consistent with the wavelengths of the high-mode internal tide. In both cases, energy advection by the mean flow does not produce a net volume-integrated energy transfer between the tide and mean flow, which explains the (nearly) offsetting regions of internal tide energy sources and sinks in Fig. 10. However, A_{mn} can facilitate energy conversion between internal tide modes via tidal scattering by the mean flow (e.g., Dunphy and Lamb 2014). This scattering appears as regions of simultaneous mode-1 energy-flux convergence and high-mode energy-flux divergence in Fig. 10.

To better identify mode-1 scattering, $\Sigma_m A_{m1}$ was low-pass filtered with a 200-km Hanning window to eliminate offsetting sources and sinks and identify net energy conversion between modes (Fig. 11). The smoothed fields vaguely indicate that the mode-1 internal tide scatters $O(1)$ mW m^{-2} to higher modes along the shoreward side of the Gulf Stream. However, these conversion rates are at least 100 times smaller than internal tide generation along the shelf break (not shown), suggesting that mode-1 scattering due to advection by the Gulf Stream is minimal.

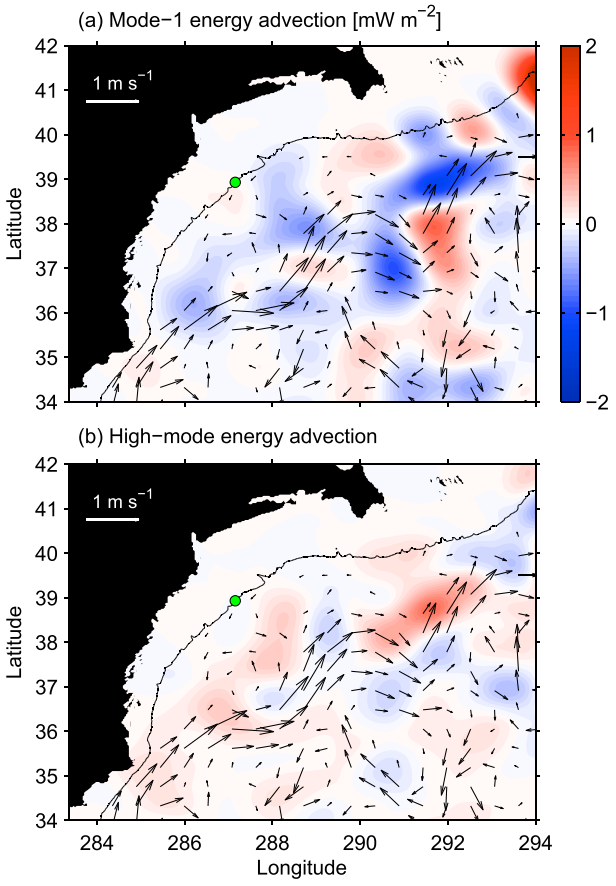

FIG. 11. Spatially smoothed tidally averaged tidal energy advection contains broad regions of $O(1)$ mW m^{-2} (a) mode-1 energy loss and (b) high-mode energy gain along the shoreward edge of the Gulf Stream. The advection fields here are obtained by smoothing the fields in Figs. 10c and 10d with a 200-km 2D Hanning window.

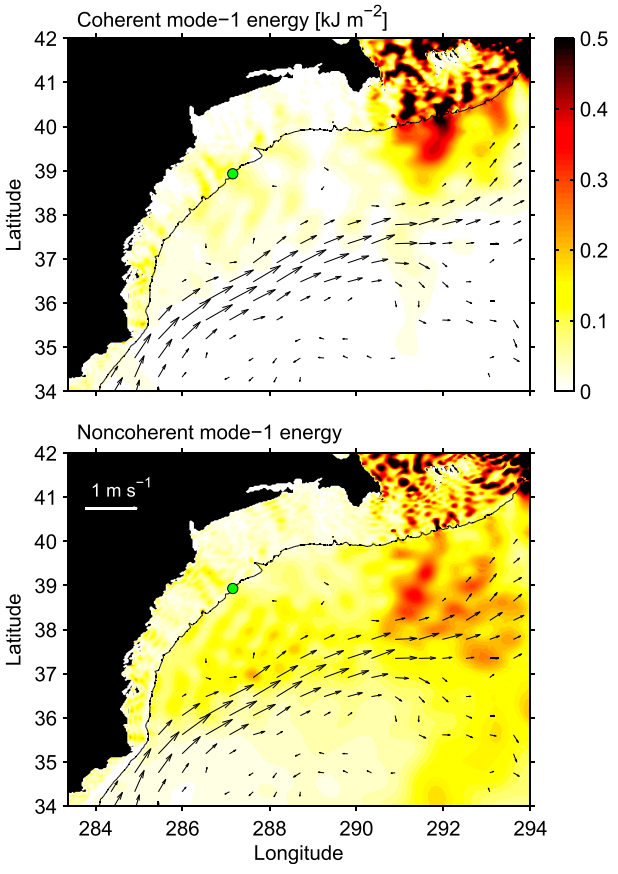

FIG. 12. CSW simulations of (a) coherent and (b) noncoherent mode-1 tidal energy are enhanced shoreward of the Gulf Stream. Coherent energy is largest in internal tide generation hotspots and noncoherent energy is largest where the internal tides propagating away from the hotspot interact, or have interacted, with the Gulf Stream.

c. *Internal tide coherence in the Mid-Atlantic Bight region*

Snapshots of internal tide pressure from individual realizations of the Gulf Stream display unique and complicated interference patterns that are difficult to interpret in terms of individual wave reflections/refraction at the Gulf Stream. However, the statistical effect of the Gulf Stream is evident from maps of coherent (stationary) and noncoherent (nonstationary) tidally averaged mode-1 energy (Fig. 12). Therefore, harmonic amplitudes at each location are decomposed into a coherent signal, defined as the 12-simulation ensemble-mean amplitude, and a noncoherent signal, defined as the residual amplitude (e.g., Zaron and Egbert 2014). Coherent energy is computed directly from the coherent harmonic amplitudes and noncoherent energy is computed as total energy minus coherent energy (Munk and Cartwright 1966; Kelly et al. 2015). Following Nash et al. (2012a), coherent energy flux is computed from the coherent amplitudes and noncoherent energy flux is computed from the noncoherent amplitudes.

Both coherent and noncoherent energies are enhanced onshore (north) of the Gulf Stream, indicating that significant mode-1 tidal energy is trapped along the continental margin by reflection at the Gulf Stream. East of George's Bank, mode-1 energy is coherent in the generation region and becomes noncoherent as it enters the Gulf Stream, indicating that accurate internal tide predictions require accurate predictions of tide–mean flow interactions. Zaron and Egbert (2014) reported a similar result for energetic internal tides radiating away from the Hawaiian Ridge. Where less energetic internal tides encounter stronger mean flows, for example, the Mid-Atlantic Bight between 35° and 40°N, noncoherent energy is larger than coherent energy, suggesting that

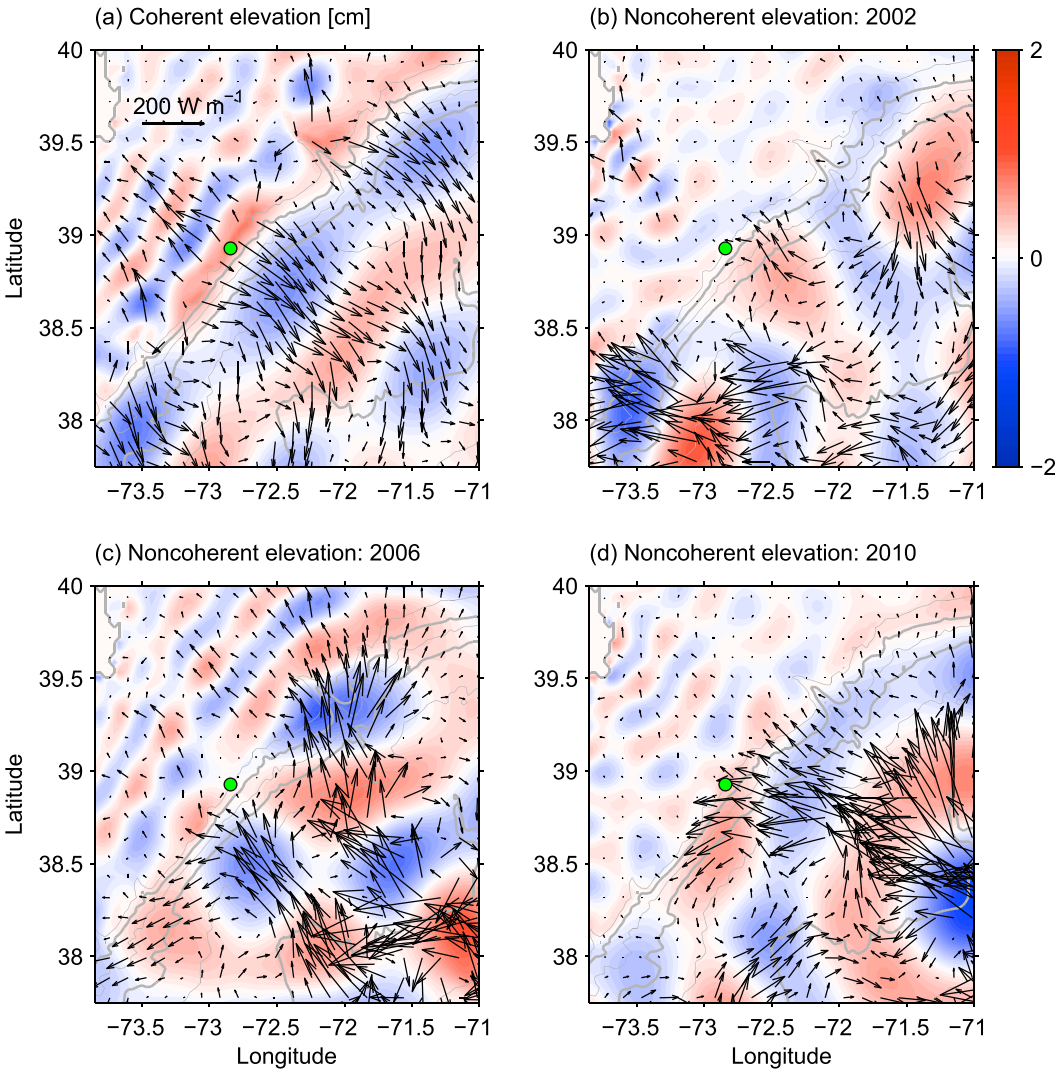

FIG. 13. Snapshots of CSW simulated (a) coherent and (b)–(d) noncoherent mode-1 surface displacements on 20 Aug display internal tide variability along the New Jersey shelf break. Energy-flux vectors computed from the coherent tide in (a) indicate energy propagation away from the shelf break, while those computed from the noncoherent tide in (b)–(d) indicate spatially heterogeneous energy propagation toward the shelf break. A green dot marks the location of the SW06 field experiment. Depth contours are shown every 500 m. Noncoherent tides from the years that are not shown are similar in character.

most of the mode-1 internal tide cannot be predicted nor analyzed using conventional tidal analyses (e.g., the harmonic or response methods; Doodson 1921; Munk and Cartwright 1966).

d. *Intermittent internal tides at the New Jersey shelf break*

Previous observations from the New Jersey shelf break, during the SW06 experiment, indicated that (i) a locally generated low-mode internal tide produces coherent offshore energy flux and (ii) a remotely generated low-mode internal tide produces intermittent onshore energy flux (Kelly and Nash 2010; Nash et al. 2012a). Moreover, the onshore energy flux of nonlinear wave packets (likely spawned from shoreward-propagating internal tides) has been observed to be spatially heterogeneous along the shelf break with a length scale of $O(20)$ km. These results are in qualitative agreement with the CSW simulations, which show the coherent, mode-1 internal tide (i) has crests and troughs in surface displacement that are aligned with the shelf break and (ii) produces energy flux that diverges along the shelf break (Fig. 13a). Conversely, the noncoherent, mode-1 internal tide (i) has sea surface displacements

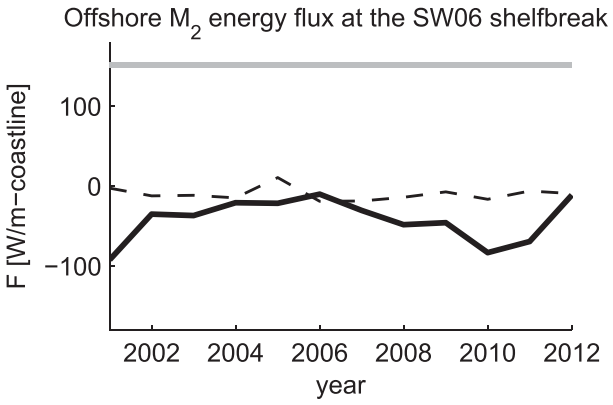

FIG. 14. A time series of CSW energy flux at the SW06 shelf break on 20 Aug of each year indicates that (i) coherent energy fluxes (gray), which are offshore, are the same magnitude regardless of the inclusion/exclusion of Gulf Stream and (ii) noncoherent energy fluxes, which are onshore, are stronger when the Gulf Stream is included (solid black) than excluded (dashed black).

that resemble a confused wavefield with no dominant directionality and (ii) produces patches of onshore energy flux that intermittently impact narrow sections of the shelf break (Figs. 13b–d).

A time series of energy flux at the SW06 study site (Fig. 14) indicates that coherent offshore energy flux is present in the simulations with and without the Gulf Stream, but noncoherent onshore energy flux is only present in the simulations with the Gulf Stream. The precise magnitude and timing of the simulated and observed onshore energy fluxes do not agree and are not expected to agree because (i) the simulations are not forced with all tidal constituents and (ii) the time-evolving, three-dimensional structure of the Gulf Stream during the SW06 experiment is not precisely known from the HYCOM fields alone.

6. Summary and conclusions

Comparisons of CSW with analytical solutions and nonlinear numerical models indicate that CSW is capable of diagnosing and simulating internal tide generation and tide–mean flow and tide–mean buoyancy interactions in realistic settings. The model is flexible enough to incorporate arbitrary topography, stratification, surface tide forcing (via the ITGF), and background conditions while operating at $<1\%$ of the computational expense of a 3D primitive equation model. This is because the slowly varying background flow and density fields are not explicitly simulated, tide–mean flow interactions are linearized, and the modal CSW equations are essentially a set of coupled 2D partial differential equations. From this perspective, CSW is useful for (i) studying high-resolution (e.g., $\Delta x \approx 1$ km) internal tidal dynamics in large computational domains and (ii) producing rapid internal tide simulations that include the effects of regional subtidal flows. However, this first-order model cannot replace a fully nonlinear model in regions with large tidal excursions, significant wave–wave interactions, or other types of nonlinear phenomena. Also, CSW presently produces instabilities in regions of strong mean flow shear, and further research is required to determine if these instabilities are due to wave capture and/or neglected higher-order terms that represent dissipation.

Nash et al. (2012a) linked the presence of nonlinear internal waves on the New Jersey shelf with bursts of onshore energy flux at the shelf break. Although they did not identify the source of onshore energy flux, they suggested two possibilities: (i) open-ocean internal tide ''swell,'' which is generated at distant topographic features, such as midocean ridges and remote continental slopes (Alford 2003), and (ii) locally generated internal tides that refract onshore due to regional topographic variability (Sherwin et al. 2002). The simulations here produced onshore energy fluxes without including extremely distant energy sources (e.g., the Mid-Atlantic Ridge, Bermuda, or the European continental slope). However, the simulations did not produce onshore energy fluxes from regional topographic variability alone. Instead, our results support a third possibility: regionally generated low-mode internal tides are modified and reflected back to the coast by the Gulf Stream. This explanation implies that coastal internal wave dynamics in the Mid-Atlantic Bight region are sensitive to the precise position and strength of the Gulf Stream and its associated meanders, warm-core rings, and eddy field. Improved predictions of internal tides and nonlinear internal waves in this region need to account for these features and their variability.

Acknowledgments. We thank G. Gawarkiewicz and P. Abbot for their AWACS-SW06 ocean data and M. Taylor and J. Hare for their NMFS survey data. We thank Dr. K. Brink and two anonymous reviewers for their many constructive suggestions. We thank the National Science Foundation for support under Grant OCE-1061160 (ShelfIT) to the Massachusetts Institute of Technology (MIT) and under Grant OCE-1060430 to the Woods Hole Oceanographic Institution. PFJL and PJH also thank the Office of Naval Research for research support under Grants N00014-11-1-0701 (MURI-IODA), N00014-12-1-0944 (ONR6.2), and N00014-13-1-0518 (Multi-DA) to MIT.

REFERENCES

Adcroft, A. J., C. N. Hill, and J. C. Marshall, 1999: A new treatment of the Coriolis terms in C-grid models at both high and low resolutions. *Mon. Wea. Rev.*, **127**, 1928–1936, doi:10.1175/1520-0493(1999)127<1928:ANTOTC>2.0.CO;2.

Alford, M. H., 2003: Redistribution of energy available for ocean mixing by long-range propagation of internal waves. *Nature*, **423**, 159–162, doi:10.1038/nature01628.

——, and Z. Zhao, 2007: Global patterns of low-mode internal-wave propagation. Part I: Energy and energy flux. *J. Phys. Oceanogr.*, **37**, 1829–1848, doi:10.1175/JPO3085.1.

——, and Coauthors, 2015: The formation and fate of internal waves in the South China Sea. *Nature*, **521**, 65–69, doi:10.1038/nature14399.

Arakawa, A., and V. R. Lamb, 1977: Computational design of the basic dynamical processes of the UCLA general circulation model. Methods in Computational Physics, J. Chang, Ed., Academic Press, 174–267.

Baines, P. G., 1982: On internal tide generation models. *Deep-Sea Res.*, **29A**, 307–338, doi:10.1016/0198-0149(82)90098-X.

Bryan, K., S. Manabe, and R. C. Pacanowski, 1975: A global ocean–atmosphere climate model. Part II. The ocean circulation. *J. Phys. Oceanogr.*, **5**, 30–46, doi:10.1175/1520-0485(1975)005<0030:AGOACM>2.0.CO;2.

Bühler, O., and M. E. McIntyre, 2005: Wave capture and wave-vortex duality. *J. Fluid Mech.*, **534**, 67–95, doi:10.1017/S0022112005004374.

Buijsman, M. C., and Coauthors, 2014: Three-dimensional double-ridge internal tide resonance in Luzon Strait. *J. Phys. Oceanogr.*, **44**, 850–869, doi:10.1175/JPO-D-13-024.1.

Carter, G. S., and Coauthors, 2008: Energetics of M_2 barotropic-to-baroclinic tidal conversion at the Hawaiian Islands. *J. Phys. Oceanogr.*, **38**, 2205–2223, doi:10.1175/2008JPO3860.1.

Chapman, N. R., and J. F. Lynch, 2010: Editorial: Special issue on the 2006 shallow water experiment. *IEEE J. Oceanic Eng.*, **35**, 1–2, doi:10.1109/JOE.2010.2040648.

Chassignet, E. P., H. E. Hurlburt, O. M. Smedstad, G. R. Halliwell, P. J. Hogan, A. J. Wallcraft, R. Baraille, and R. Bleck, 2007: The HYCOM (Hybrid Coordinate Ocean Model) data assimilative system. *J. Mar. Syst.*, **65**, 60–83, doi:10.1016/j.jmarsys.2005.09.016.

Chen, C. H., and Coauthors, 2011: Tidal dynamics in the Gulf of Maine and New England shelf: An application of FVCOM. *J. Geophys. Res.*, **116**, C12010, doi:10.1029/2011JC007054.

Colin, M. E. G. D., and Coauthors, 2013: Time-evolving acoustic propagation modeling in a complex ocean environment. *OCEANS 2013*, Bergen, Norway, IEEE/MTS, 1–9, doi:10.1109/OCEANS-Bergen.2013.6608051.

Colosi, J. A., R. C. Beardsley, J. F. Lynch, G. Gawarkiewicz, C.-S. Chiu, and A. Scotti, 2001: Observations of nonlinear internal waves on the outer New England continental shelf during the summer Shelfbreak Primer study. *J. Geophys. Res.*, **106**, 9587–9601, doi:10.1029/2000JC900124.

——, T. F. Duda, Y.-T. Lin, J. F. Newhall, E. Arthur, and B. D. Cornuelle, 2012: Observations of sound-speed fluctuations on the New Jersey continental shelf in the summer of 2006. *J. Acoust. Soc. Amer.*, **131**, 1733–1748, doi:10.1121/1.3666014.

Cushman-Roisin, B., and J.-M. Beckers, 2011: *Introduction to Geophysical Fluid Dynamics*. 2nd ed. Academic Press, 875 pp.

Doodson, A., 1921: The harmonic development of the tide-generating potential. *Proc. Roy. Soc. London*, **100**, 305–329, doi:10.1098/rspa.1921.0088.

Duda, T. F., and Coauthors, 2014: Issues and progress in the prediction of ocean submesoscale features and internal waves. *OCEANS '14*, Taipei, Taiwan, IEEE/MTS, 1–9. [Available online at http://mseas.mit.edu/publications/PDF/DudaEtal_Issues_Prog_submeso_IWs_OceansIEEE2014.pdf.]

Dunphy, M., and K. G. Lamb, 2014: Focusing and vertical mode scattering of the first mode internal tide by mesoscale eddy interaction. *J. Geophys. Res. Oceans*, **119**, 523–536, doi:10.1002/2013JC009293.

Egbert, G. D., 1997: Tidal data inversion: Interpolation and inference. *Prog. Oceanogr.*, **40**, 53–80, doi:10.1016/S0079-6611(97)00023-2.

Garrett, C., and E. Kunze, 2007: Internal tide generation in the deep ocean. *Annu. Rev. Fluid Mech.*, **39**, 57–87, doi:10.1146/annurev.fluid.39.050905.110227.

Gayen, B., and S. Sarkar, 2011: Direct and large-eddy simulations of internal tide generation at a near-critical slope. *J. Fluid Mech.*, **681**, 48–71, doi:10.1017/jfm.2011.170.

Gill, A. E., and A. J. Clarke, 1974: Wind-induced upwelling, coastal currents and sea-level changes. *Deep-Sea Res. Oceanogr. Abstr.*, **21**, 325–345, doi:10.1016/0011-7471(74)90038-2.

Griffiths, S. D., and R. H. J. Grimshaw, 2007: Internal tide generation at the continental shelf modeled using a modal decomposition: Two-dimensional results. *J. Phys. Oceanogr.*, **37**, 428–451, doi:10.1175/JPO3068.1.

Haley, P. J., Jr., and P. F. Lermusiaux, 2010: Multiscale two-way embedding schemes for free-surface primitive equations in the "multidisciplinary simulation, estimation and assimilation system." *Ocean Dyn.*, **60**, 1497–1537, doi:10.1007/s10236-010-0349-4.

Hendershott, M. C., 1981: Long waves and ocean tides. Evolution of Physical Oceanography: Scientific Surveys in Honor of Henry Stommel, B. A. Warren and C. Wunsch, Eds., MIT Press, 292–341.

Hollaway, P. E., 1988: Climatology of internal tides at a shelf-break location on the Australian North West Shelf. *Aust. J. Mar. Freshwater Res.*, **39**, 1–18, doi:10.1071/MF9880001.

Holloway, P. E., 1984: On the semidiurnal internal tide at a shelf-break region on the Australian North West Shelf. *J. Phys. Oceanogr.*, **14**, 1787–1799, doi:10.1175/1520-0485(1984)014<1787:OTSITA>2.0.CO;2.

Huthnance, J. M., 1995: Circulation, exchange and water masses at the ocean margin: The role of physical processes at the shelf edge. *Prog. Oceanogr.*, **35**, 353–431, doi:10.1016/0079-6611(95)80003-C.

Ivey, G. N., 2011: Tides and internal waves on the continental shelf. *Operational Oceanography in the 21st Century*, A. Schiller and G. B. Brassington, Eds., Springer, 225–235.

Jackson, C., 2004: *An Atlas of Oceanic Internal Solitary-Like Waves and Their Properties*. Global Ocean Associates, Office of Naval Research Code 322PO, Contract N00014-03-C-0176, accessed 2 September 2012. [Available online at http://www.internalwaveatlas.com/Atlas2_index.html.]

Kang, D., and O. Fringer, 2012: Energetics of barotropic and baroclinic tides in the Monterey Bay area. *J. Phys. Oceanogr.*, **42**, 272–290, doi:10.1175/JPO-D-11-039.1.

Kelly, S. M., 2016: The vertical mode decomposition of surface and internal tides in the presence of a free surface and arbitrary topography. *J. Phys. Oceanogr.*, doi:10.1175/JPO-D-16-0131.1, in press.

——, and J. D. Nash, 2010: Internal-tide generation and destruction by shoaling internal tides. *Geophys. Res. Lett.*, **37**, L23611, doi:10.1029/2010GL045598.

——, and P. F. J. Lermusiaux, 2016: Internal-tide interactions with the Gulf Stream and Middle Atlantic Bight shelfbreak front. *J. Geophys. Res. Oceans*, **121**, 6271–6294, doi:10.1002/2016JC011639.

——, J. D. Nash, and E. Kunze, 2010: Internal-tide energy over topography. *J. Geophys. Res.*, **115**, C06014, doi:10.1029/2009JC005618.

——, ——, K. I. Martini, M. H. Alford, and E. Kunze, 2012: The cascade of tidal energy from low to high modes on a continental slope. *J. Phys. Oceanogr.*, **42**, 1217–1232, doi:10.1175/JPO-D-11-0231.1.

——, N. L. Jones, and J. D. Nash, 2013: A coupled model for Laplace's tidal equations in a fluid with one horizontal dimension and variable depth. *J. Phys. Oceanogr.*, **43**, 1780–1797, doi:10.1175/JPO-D-12-0147.1.

——, ——, G. I. Ivey, and R. N. Lowe, 2015: Internal tide spectroscopy and prediction in the Timor Sea. *J. Phys. Oceanogr.*, **45**, 64–83, doi:10.1175/JPO-D-14-0007.1.

Kurapov, A. L., G. Egbert, J. S. Allen, R. N. Miller, S. Y. Erofeeva, and P. M. Kosro, 2003: The M_2 internal tide off Oregon: Inferences from data assimilation. *J. Phys. Oceanogr.*, **33**, 1733–1757, doi:10.1175/2397.1.

——, J. S. Allen, and G. D. Egbert, 2010: Combined effects of wind-driven upwelling and internal tide on the continental shelf. *J. Phys. Oceanogr.*, **40**, 737–756, doi:10.1175/2009JPO4183.1.

Lamb, K. G., 2004: Nonlinear interaction among internal wave beams generated by tidal flow over supercritical topography. *Geophys. Res. Lett.*, **31**, L09313, doi:10.1029/2003GL019393.

——, 2014: Internal wave breaking and dissipation mechanisms on the continental slope/shelf. *Annu. Rev. Fluid Mech.*, **46**, 231–254, doi:10.1146/annurev-fluid-011212-140701.

Lavelle, J. W., and W. C. Thacker, 2008: A pretty good sponge: Dealing with open boundaries in limited-area ocean models. *Ocean Modell.*, **20**, 270–292, doi:10.1016/j.ocemod.2007.10.002.

Legg, S., and K. M. H. Huijts, 2006: Preliminary simulations of internal waves and mixing generated by finite amplitude tidal flow over isolated topography. *Deep-Sea Res.*, **53**, 140–156, doi:10.1016/j.dsr2.2005.09.014.

Lerczak, J., C. Winant, and M. Hendershott, 2003: Observations of the semidiurnal internal tide on the southern California slope and shelf. *J. Geophys. Res*, **108**, 3068, doi:10.1029/2001JC001128.

Lermusiaux, P. F. J., P. J. Haley Jr., W. G. Leslie, O. Logoutov, and A. R. Robinson, 2006: Autonomous Wide Aperture Cluster for Surveillance (AWACS): Adaptive sampling and search using predictive models with coupled data assimilation and feedback. Harvard University, accessed 12 January 2016. [Available online at http://mseas.mit.edu/archive/AWACS/index_AWACS.html.]

Lin, Y.-T., A. E. Newhall, T. F. Duda, P. F. J. Lermusiaux, and P. J. Haley Jr., 2010: Merging multiple-partial-depth data time series using objective empirical orthogonal function fitting. *IEEE J. Oceanic Eng.*, **35**, 710–721, doi:10.1109/JOE.2010.2052875.

Lynch, J., and D. Tang, 2008: Overview of shallow water 2006 *JASA EL* special issue papers. *J. Acoust. Soc. Amer.*, **124**, EL63–EL65, doi:10.1121/1.2972156.

Marshall, J., A. Adcroft, C. Hill, L. Perelman, and C. Heisey, 1997: A finite-volume, incompressible Navier Stokes model for studies of the ocean on parallel computers. *J. Geophys. Res.*, **102**, 5753–5766, doi:10.1029/96JC02775.

Moum, J. N., and J. D. Nash, 2008: Seafloor pressure measurements of nonlinear internal waves. *J. Phys. Oceanogr.*, **38**, 481–491, doi:10.1175/2007JPO3736.1.

Munk, W. H., and D. E. Cartwright, 1966: Tidal spectroscopy and prediction. *Philos. Trans. Roy. Soc. London*, **259**, 533–581, doi:10.1098/rsta.1966.0024.

Nash, J. D., E. Kunze, C. M. Lee, and T. B. Sanford, 2006: Structure of the baroclinic tide generated at Kaena Ridge, Hawaii. *J. Phys. Oceanogr.*, **36**, 1123–1135, doi:10.1175/JPO2883.1.

——, S. M. Kelly, E. L. Shroyer, J. N. Moum, and T. F. Duda, 2012a: The unpredictable nature of internal tides on continental shelves. *J. Phys. Oceanogr.*, **42**, 1981–2000, doi:10.1175/JPO-D-12-028.1.

——, E. Shroyer, S. M. Kelly, M. Inall, T. Duda, M. Levine, N. Jones, and R. Musgrave, 2012b: Are any coastal internal tides predictable? *Oceanography*, **25**, 80–95, doi:10.5670/oceanog.2012.44.

Newhall, A. E., and Coauthors, 2007: Acoustic and oceanographic observations and configuration information for the WHOI moorings from the SW06 experiment. WHOI Tech. Rep. WHOI-2007-04, 119 pp. [Available online at http://hdl.handle.net/1912/1826.]

Park, J., and D. R. Watts, 2006: Internal tides in the southwestern Japan/East Sea. *J. Phys. Oceanogr.*, **36**, 22–34, doi:10.1175/JPO2846.1.

Pedlosky, J., 2003: *Waves in the Ocean and Atmosphere*. 1st ed. Springer, 183–191.

Rainville, L., and R. Pinkel, 2006: Propagation of low-mode internal waves through the ocean. *J. Phys. Oceanogr.*, **36**, 1220–1236, doi:10.1175/JPO2889.1.

Sharples, J., and Coauthors, 2007: Spring-neap modulation of internal tide mixing and vertical nitrate fluxes at a shelf edge in summer. *Limnol. Oceanogr.*, **52**, 1735–1747, doi:10.4319/lo.2007.52.5.1735.

Sherwin, T. J., V. I. Vlasenko, N. Stashchuk, D. R. Jeans, and B. Jones, 2002: Along-slope generation as an explanation for some unusually large internal tides. *Deep-Sea Res. I*, **49**, 1787–1799, doi:10.1016/S0967-0637(02)00096-1.

Shroyer, E. L., J. N. Moum, and J. D. Nash, 2009: Observations of polarity reversal in shoaling nonlinear internal waves. *J. Phys. Oceanogr.*, **39**, 691–701, doi:10.1175/2008JPO3953.1.

——, ——, and ——, 2010a: Energy transformations and dissipation of nonlinear internal waves over New Jersey's continental shelf. *Nonlinear Processes Geophys.*, **17**, 345–360, doi:10.5194/npg-17-345-2010.

——, ——, and ——, 2010b: Mode 2 waves on the continental shelf: Ephemeral components of the nonlinear internal wavefield. *J. Geophys. Res.*, **115**, C07001, doi:10.1029/2009JC005605.

——, ——, and ——, 2010c: Vertical heat flux and lateral transport in nonlinear internal waves. *Geophys. Res. Lett.*, **37**, L08601, doi:10.1029/2010GL042715.

——, ——, and ——, 2011: Nonlinear internal waves over New Jersey's continental shelf. *J. Geophys. Res.*, **116**, C03022, doi:10.1029/2010JC006332.

Smith, W. H. F., and D. T. Sandwell, 1997: Global sea floor topography from satellite altimetry and ship depth soundings. *Science*, **277**, 1956–1962, doi:10.1126/science.277.5334.1956.

Tang, D., and Coauthors, 2007: Shallow Water '06: A joint acoustic propagation/nonlinear internal wave physics experiment. *Oceanography*, **20**, 156–167, doi:10.5670/oceanog.2007.16.

Venayagamoorthy, S. K., and O. B. Fringer, 2006: Numerical simulations of the interaction of internal waves with a shelf break. *Phys. Fluids*, **18**, 076603, doi:10.1063/1.2221863.

Zaron, E. D., and G. D. Egbert, 2014: Time-variable refraction of the internal tide at the Hawaiian Ridge. *J. Phys. Oceanogr.*, **44**, 538–557, doi:10.1175/JPO-D-12-0238.1.

Zhang, Y. G., and T. F. Duda, 2013: Intrinsic nonlinearity and spectral structure of internal tides at an idealized Mid-Atlantic Bight shelf break. *J. Phys. Oceanogr.*, **43**, 2641–2660, doi:10.1175/JPO-D-12-0239.1.